The vertical distribution of ozone in Mars Years 34-35 from ExoMars TGO/NOMAD-UVIS observations

M.R. Patel[1,2], G. Sellers[1], J.P. Mason[1], J.A. Holmes[1], M.A.J. Brown[1], S.R. Lewis[1], K. Rajendran[1], P.M. Streeter[1], C. Marriner[1], B.G. Hathi[1], D.J. Slade[1], M.R. Leese[1], M.J. Wolff[3], A.S.J. Khayat[4,5], M.D. Smith[4], S. Aoki[6,9], A. Piccialli[6], A.C. Vandaele[6], S. Robert[6,10], F. Daerden[6], I. R. Thomas[6], B. Ristic[6], Y. Willame[6], C. Depiesse[6], G. Bellucci[7], J.-J. Lopez-Moreno[8] and the NOMAD team

[1] School of Physical Sciences, The Open University, Milton Keynes, U.K.

[2] Space Science and Technology Department, Science and Technology Facilities Council, Rutherford Appleton Laboratory, Oxfordshire, U.K.

[3] Space Science Institute, 4750 Walnut Street, Suite 205, Boulder, CO 80301, UCB 564, USA.

[4] NASA Goddard Space Flight Center, Greenbelt, MD 20771, USA.

[5] Center for Research and Exploration in Space Science and Technology II, University of Maryland, College Park, USA.

[6] Royal Belgian Institute for Space Aeronomy, BIRA-IASB, 3 Avenue Circulaire, 1180 Brussels, Belgium.

[7] Istituto di Astrofisica e Planetologia Spaziali, IAPS-INAF, Via del Fosso del Cavaliere 100, 00133 Rome, Italy.

[8] Instituto de Astrofisica de Andalucia, IAA-CSIC, Glorieta de la Astronomia, 18008 Granada, Spain.

[9] LPAP, STAR Institute, Université de Liège, Allée du 6 août, 19C, 4000 Liège, Belgium

[10] Institute of Condensed Matter and Nanosciences, Université catholique de Louvain, Chemin du Cyclotron 2, 1348 Louvain-la-Neuve, Belgium

Corresponding author: Manish Patel, email: manish.patel@open.ac.uk

Key Points:

- The annual martian ozone distribution has been measured with high vertical resolution.
- High altitude equinoctial ozone enhancements periodically occur on Mars at altitudes of ~50 km.
- These high altitude ozone enhancements form in both hemispheres at both vernal and autumnal equinoxes.

Abstract

We present ~1.5 Mars Years (MY) of ozone vertical profiles, covering L_S = 163° in MY34 to L_S = 320° in MY35, a period which includes the 2018 global dust storm. Since April 2018, the Ultraviolet and Visible Spectrometer (UVIS) channel of the Nadir and Occultation for Mars Discovery (NOMAD) spectrometer aboard the ExoMars Trace Gas Orbiter has observed the vertical, latitudinal and seasonal distributions of ozone. Around perihelion, the relative abundance of ozone (and water from coincident NOMAD measurements) increases strongly together below ~40 km. Around aphelion, decreases in ozone abundance exist between 25-35 km coincident with the location of modelled peak water abundances. We report high latitude (> ± 55°), high altitude (40-55 km) equinoctial ozone enhancements in both hemispheres. The northern equinoctial high altitude enhancement is previously unobserved and forms prior to vernal equinox lasting for almost 100 sols (L_S ~350-40°), whereas the southern enhancement persists for over twice as long (L_S = ~5-140°). Both layers reform at autumnal equinox, with the northern layer at a lower abundance. These layers likely form through a combination of anti-correlation with water and the equinoctial meridional transport of O and H atoms to high-latitude regions. The descending branch of the main Hadley cell shapes the ozone distribution at L_S = 40-60°, with the possible signature of a northern hemisphere thermally indirect cell identifiable from L_S = 40-80°. The ozone retrievals presented here provide the most complete global description of Mars ozone vertical distributions as a function of season and latitude.

Plain Language Summary

We present over two years of new observations of the vertical distribution of ozone in the atmosphere of Mars. The ExoMars Trace Gas Orbiter spacecraft has been making observations of the martian atmosphere since 2018 to map the presence and changes in abundance of gases such as ozone by using the 'NOMAD' instrument. NOMAD continually observes the change in ozone abundance (among other gases) with height across much of the planet. These abundance profiles have revealed the presence of distinct layers of ozone enhancement at high altitudes in the atmosphere of Mars towards the polar regions and between spring and autumn in the southern hemisphere of Mars. The abundance of ozone is linked to the abundance of water vapour through chemical reactions, with an increase in water usually leading to a decrease in ozone. We observe broad periods where often the abundance of ozone follows the abundance of water from ~10 km altitude up to ~50 km altitude, and other times when the two appear to be opposite in their variation with height. Our retrievals of ozone from NOMAD data provide the first coincident observations of ozone and water and provide previously unavailable information on the photochemistry of Mars.

1 Introduction

Ozone (O_3) is a highly reactive trace gas in the martian atmosphere, where odd-hydrogen (OH, HO_2, H, H_2O_2) catalytic products of water vapor photolysis dominate Mars photochemistry (Parkinson and Hunten, 1972; McElroy and Donahue, 1972), and contribute the primary loss mechanism for Mars O_3. As a consequence, large spatial and temporal changes in Mars O_3 were quickly recognized to be associated with condensation-driven variations in atmospheric water vapour (Barth et al., 1973; Kong and McElroy, 1977, Shimazaki and Shimizu, 1979; Clancy and Nair, 1996). Mars atmospheric water variations result from seasonal/spatial variations in loss or supply to seasonal and residual polar ice caps (Jakosky and Farmer, 1982; Smith, 2004, 2009; Fedorova et al., 2006; Steele et al., 2014; Pankine and Tamppari, 2019); and by the large

spatial/temporal variations in ice cloud saturation conditions in the Mars atmosphere (Clancy et al, 1996; Montmessin et al., 2004; Navarro et al., 2014; Neary et al., 2020).

Mariner 7 made the first detection of O_3 in the martian atmosphere (Barth and Hord, 1971) and later Mariner 9 showed O_3 to be seasonally variable (Barth et al., 1973). Subsequent missions and ground-based observations have characterised the geographical and seasonal variability of O_3 extensively (e.g. Blamont and Chassefière, 1993; Clancy et al. 1999; Fast et al., 2006; Perrier et al. 2006; Lebonnois et al., 2006; Montmessin and Lefèvre, 2013; Clancy et al. 2016; Lefèvre et al., 2017). This has led to the well-established O_3 climatology of increased column abundances in the cold, dry atmospheric conditions of the fall and winter high latitude regions; and reduced substantially in abundance over warmer, wetter low latitude and summer high latitude regions. In addition, a distinct-low latitude, mid-altitude peak in O_3 arises from ~20 K colder atmospheric (and surface) temperatures present around Mars aphelion (Clancy and Nair, 1996), when Mars is furthest from the Sun in its eccentric orbit (at the current epoch, this occurs around Mars northern summer at a solar longitude, L_S, of 71°). These basic temporal and spatial behaviours of Mars atmospheric O_3 and H_2O column abundances are qualitatively reproduced in Mars global circulation models (GCM) (e.g. Lefèvre et al. 2004, 2008; Holmes et al, 2017; Holmes et al, 2018; Holmes et al, 2020; Daerden et al., 2019).

However, most of the above behaviours are primarily characterized in terms of column O_3 measurements, due to the limited extent of vertical profile measurements for O_3 (Lebonnois et al., 2006; Clancy et al., 2017) or H_2O (Maltagliati et al., 2013; Fedorova et al, 2018). This is a significant limitation given the importance of vertical profile dependences in characterizing these photochemical and water vapor saturation (cloud microphysical) processes in any detail. Surprisingly, our understanding of such a fundamental relationship as the anti-correlation of Mars atmospheric O_3 and H_2O is obscured by uncertainties associated with column O_3 and H_2O measurement comparisons. Current model-data comparisons for these column data sets have implied significant (50-100%) excesses in observed atmospheric O_3, while reproducing observed water column abundances more closely (Lefèvre et al., 2008). Heterogenous reduction of HO_x on Mars water ice clouds has been proposed to account for such elevated O_3 abundances relative to homogeneous (gas-phase only) photochemical predictions (Lefèvre el al., 2008). Subsequent Mars O_3 observations have not yet indicated a heterogenous solution but the model underestimations of O_3 columns remain unresolved (Clancy et al., 2016; Daerden et al., 2019). It is possible, perhaps likely, that inaccurate model simulations of water vapor (and O_3) profiles contributes significantly to this issue (Clancy et al., 2017). Column O_3 measurements are heavily weighted by O_3 abundances in the lower scale height (~10 km), a region untouched by profile measurements to date. Column H_2O measurements do not provide significant guidance to temperature-sensitive, process-complicated simulations of cloud microphysics, necessary to simulate water vapor profiles accurately (e.g., Navarro et al., 2014).

Consequently, ExoMars TGO sensitive and accurate determinations for O_3 profiles through UV (260 nm Hartley band) solar occultations (this paper), and water vapor profiles through near-IR solar occultations (NOMAD- Vandaele et al., 2019, Aoki et al., 2020; ACS- Fedorova et al., 2020), represents a major observational advance in the study of Mars photochemistry. On their own, NOMAD O_3 profile retrievals yield a unique vertical dimension to our definition of Mars photochemistry. Coincident with NOMAD water profile retrievals, they enable an intrinsically diagnostic study of Mars O_x ($O + O_3$) and HO_x chemistry. Remaining contradictions on the presence of atmospheric methane (Korablev et al, 2019) and recent ExoMars detections of

atmospheric HCl (Korablev et al., 2020; Aoki et al., 2020) lead to renewed importance in establishing a detailed understanding of Mars photochemistry.

Here, we present retrieved NOMAD O_3 profiles, with an emphasis on generating a global view of Mars photochemistry (O_3) in the vertical dimension. Preliminary comparisons of these NOMAD O_3 profile retrievals are provided with published NOMAD water profile retrievals (over L_S = 163-345° in MY34, Aoki et al., 2019) and modelled water profiles (Holmes et al., 2020) extending over the remaining L_S range of presented O_3 profiles. An initial comparison of modelled O_3 profiles indicates the degree to which existing models, without assimilated NOMAD water profile retrievals, correspond to the NOMAD O_3 profile measurements. Following studies of the combined NOMAD water and O_3 profile data sets will employ data assimilation of NOMAD water profile measurements to fully realize anticipated advances in Mars photochemistry associated with NOMAD O_3 and H_2O profile data.

Vertical profile measurements by the Nadir and Occultation for MArs Discovery (NOMAD) spectrometer suite, aboard the ESA/Roscosmos ExoMars Trace Gas Orbiter (TGO) mission have now been taken for over 1 Mars Year (MY), allowing the first glimpse into the vertical distribution of O_3 in the atmosphere of Mars. This work is undertaken in parallel to a companion study performed using the same observations from the NOMAD/UVIS instrument (Khayat et al., this issue). A comparison of the results from the two studies is provided in the supplementary material, showing that both datasets are in general agreement. An additional study of O_3 retrievals is also being prepared within the NOMAD team, but not compared here. In this paper, we present O_3 vertical profiles from April 2018 to November 2020, covering over 1 MY of O_3 measurements. This period includes the MY34 global dust storm, as well as the occurrence of a regional storm (Guzewich et al. 2019). The details of the NOMAD observations and the retrievals method are described in sections 2 and 3 respectively, and the observational results are discussed in section 4.

2 Observations

2.1 ExoMars and NOMAD-UVIS

The Ultraviolet and Visible Spectrometer (UVIS) is one of three channels that comprise the NOMAD spectrometer suite, aboard ExoMars TGO. The other two channels of NOMAD are infrared (IR) spectrometers: the Solar Occultation (SO) channel and the Limb Nadir and Occultation (LNO) channel. A full description of the SO and LNO channels can be found in Vandaele *et al.* (2015). UVIS covers the spectral range of 200-650 nm with a spectral resolution of < 2 nm and is capable of observations in both solar occultation and nadir viewing geometries using a single spectrometer with the aim to provide a comprehensive understanding of the climatology and vertical distribution of ozone, dust aerosols and ice aerosols in the martian atmosphere. The occultation channel provides the capability to not only measure these species in the vertical and spatial dimension but to also measure changes on seasonal and diurnal timescales. A full description of the NOMAD-UVIS channel can be found in Patel *et al.* (2017)

TGO is in a near-circular 74° inclined orbit with a periapsis of 380 km and apoapsis of 420 km and an orbital period of approximately 2 hours. NOMAD occultations come in four flavours: two different pointing modes and two different spacecraft manoeuvres. When the beta angle, the angle between the normal to the orbital plane and the direction to the Sun, is <20° TGO will actively track the Sun during an occultation, keeping the instrument boresight fixed on the Sun

centre. Within each planning period (approximately 1 month) around two of these suntracking occultations will be led using the UVIS boresight (i.e. the UVIS boresight is held centred on the Sun centre); the rest are led by the NOMAD SO IR channel. At beta angles >20°, spacecraft angular momentum constraints prohibit suntracking and TGO rotates around the instrument pointing vector. This has minimal effect on UVIS-led occultations, however, on SO-led occultations the UVIS boresight traces an arc around the solar disc at a distance from the solar centre of approximately 0.3 solar radii.

2.2 Data set

Data acquired by the UVIS spectrometer from the start of the TGO science phase in April 2018 to November 2020 were used in this study, covering a period of just over one full martian year (MY 34, L_S = 163° to MY 35, L_S = 320°). This dataset comprises 5990 solar occultations (3051 egresses, 2939 ingresses) and corresponds to the Level 1.0 data made available through the NOMAD PI institute. The derived retrieval data dataset can be accessed freely through the Open Research Data Online (ORDO) repository at https://ordo.open.ac.uk/collections/NOMAD-UVIS/5269202 (DOI: https://doi.org/10.21954/ou.rd.13580336).

The geographical distribution of the occultation measurements is shown Figure 1. Due to TGO's orbital characteristics and the terminator geometry for solar occultations, the majority of occultations are to be found clustered symmetrically around ±63° latitude bands (Figure 1) in the northern and southern hemispheres, with minimally slanted (vertical) atmospheric profiles. Relatively few occultations penetrate the equatorial latitudes; those that do tend to exhibit very long ground tracks reflecting a highly slanted atmospheric profile.

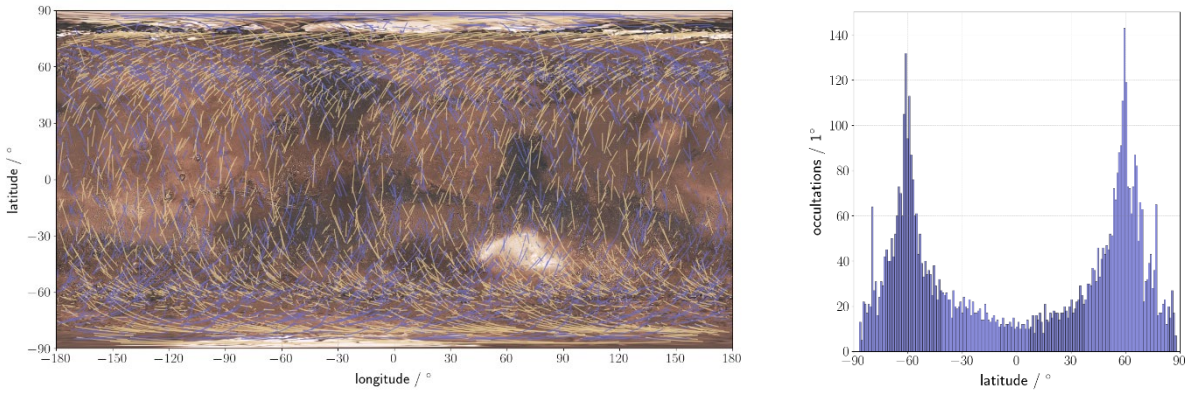

Figure 1. (left) Geographical coverage of UVIS occultation profiles represented as tangent point projected onto the martian surface, for egress occultations (yellow) and ingress occultations (blue). (right) histogram of the latitude of all occultations taken to date (latitude defined as the mid-point of the total occultation ground-track).

The latitudinal progression of the occultations over the duration of the current dataset is shown in Figure 2 and is controlled by the changing beta-angle of the spacecraft orbit. The beta angle varies in a cyclic pattern, moving between low beta angle and high beta angle phases. At low beta angles an orbit will typically consist of both an ingress and egress occultation, alternating between high latitudes in the northern and southern hemispheres. As the beta angle increases the occultations tend towards equatorial latitudes until the orbital geometry (beta angles > 60°) prohibits occultation pointing and results in a period of no occultation observations.

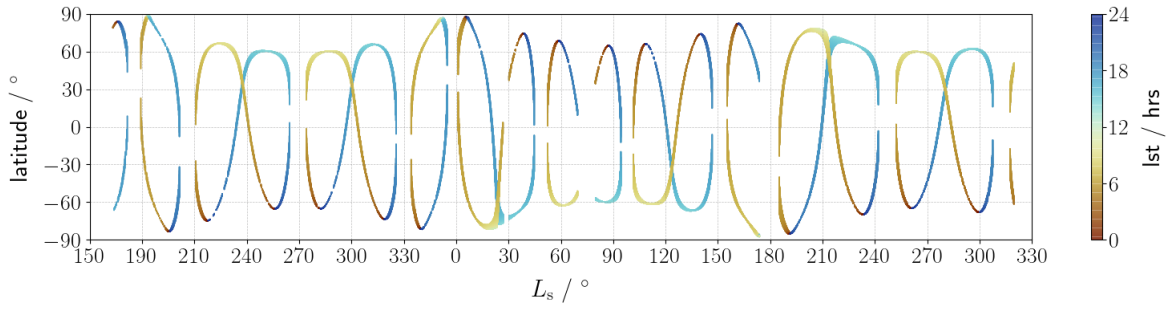

Figure 2. Latitude and local solar time variation of UVIS occultation measurements over time in solar longitude L_S.

Each individual occultation occurs over a period of between approximately 1–7 minutes, with equatorial occultations generally having longer durations as a result of the longer slant paths. The total integration time of each individual measurement was 45 ms or 75 ms. In the initial phase of the science mission (L_S = 163-345°) the UVIS sampling frequency was set to 3 s providing a spectral resolution of < 2 nm. Since the altitude resolution is also dependent on the occultation duration, the 3 s sampling frequency initially gave vertical resolutions that varied between 0.7 km and 4.4 km. This somewhat coarse altitude resolution for occultations with short durations was a result of the 3 s measurement rhythm which is set by the CCD readout time and the data transfer time from UVIS to the NOMAD data processing unit. The CCD read time is fixed and cannot be changed but the data transfer time can be reduced by sending less data. After L_S = 345°, UVIS was modified to spectrally bin the CCD array from 1024 pixels to 128 pixels, a factor of 8 reduction in the data volume, allowing an increase in the sampling frequency to 1 s, a factor of three improvement, and a corresponding increase to the altitude resolution in the range 0.2 km to 1.4 km. The spectral features of ozone, water ice aerosols, and dust aerosols are all broad band features, as such an increase in the spectral resolution to 4 nm had no impact on the retrievals.

A great benefit of the solar occultation technique is that it does not rely on laboratory radiometric calibration, and it is a self-calibrating measurement. During a solar occultation, the line of sight (LoS) between the instrument and the Sun is maintained as the LoS passes through the atmosphere, from a very high altitude (200-250 km) down to the surface (or vice versa). Relative transmission is then calculated using a reference spectrum obtained from high up in the atmosphere where no atmospheric contribution is expected (typically ~110 km), resulting in a consistently self-calibrated transmission profile through the atmosphere for each individual occultation.

2.3 Atmospheric Transmittance

This transmission is defined as the spectral radiance observed through the atmosphere at a given tangent altitude, z, above the surface, $S(\lambda, z)$, taken as a proportion of the total (above atmosphere) solar radiance, $S_0(\lambda)$.

$$T(\lambda, z) = \frac{S(\lambda, z)}{S_0(\lambda)}$$

$S_0(\lambda)$ is determined using the algorithm defined by Trompet et al. (2016), as discussed in Vandaele et al. (2018) as the standard occultation procedure for NOMAD transmissions. This method uses an iterative algorithm to define a best-fit linear regression for spectra above 120 km, where it is assumed there is no absorption due to martian atmospheric gases, thus defining a unique reference for each occultation.

The spectral transmission obtained from the data can be related to the number density of all absorbing agents in the LoS through the atmosphere through the Beer-Lambert law:

$$S(\lambda, z) = S_0(\lambda) e^{-\Sigma_i \sigma_i N_i(z)}$$

where, σ_i is the cross-section of the i^{th} absorbing chemical species and $N_i = \int n_i . dx$ is the integrated total number density per species along the LoS column. A single transmission spectrum yields a transmission ratio for each wavelength in the detector range of 200–650 nm at a spectral resolution varying between approximately 0.5–3.5 nm. An example of the corresponding set of transmission spectra obtained during a single occultation is shown in Figure 3, representing the observed transmission through different layers of the martian atmosphere.

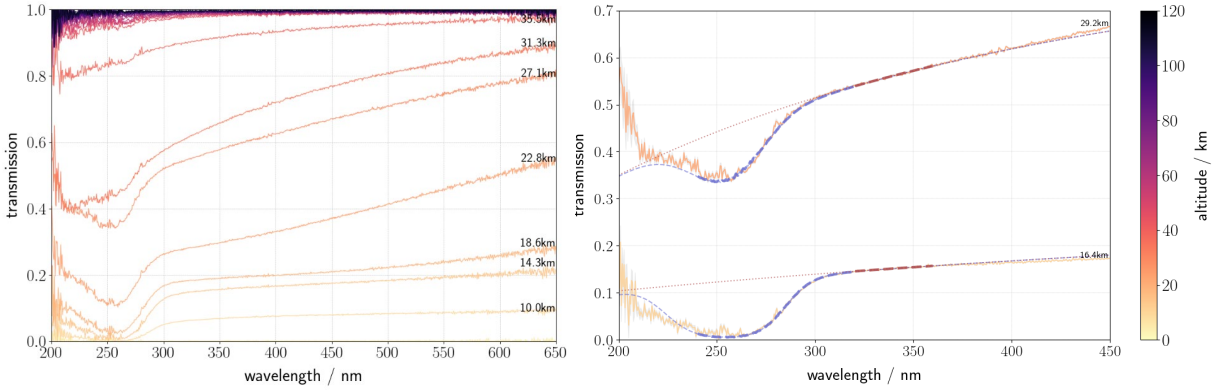

Figure 3. (left) Transmission spectra at different tangent altitudes for an example UVIS occultation. (right) Transmission spectra for a few altitudes in occultation file 20180426_141656, with aerosol fit between 320–360 nm (thick dashed red), extrapolation (dotted red), subsequent 240–320 nm O_3 fit (thick dash purple) to the observed transmission and associated uncertainty (grey region), with the final modelled transmission (thin purple dash), showing a clear identification of O_3 by the algorithm. The poor fit quality <240 nm should be disregarded since these observation data are not used in these retrievals, due to the poor quality of the instrument data at these wavelengths.

3 Retrieval method

3.1 Spectral Inversion

The transmission spectra observed by the instrument at successive tangent altitudes above the surface are converted into number densities of different species by a spectral inversion process. These number density profiles, or slant densities, are a measure of the total integrated number of a given species in the line-of-sight column of each observation.

3.1.1 The line-of-sight points

A schematic of the location of the LoS between the TGO spacecraft and the Sun for each observation is shown in Figure 4. The tangent height point, denoted by $\mathbf{X}_{tan}$, is defined as the point along the LoS that has the shortest distance from the LoS to the centre of the planet.

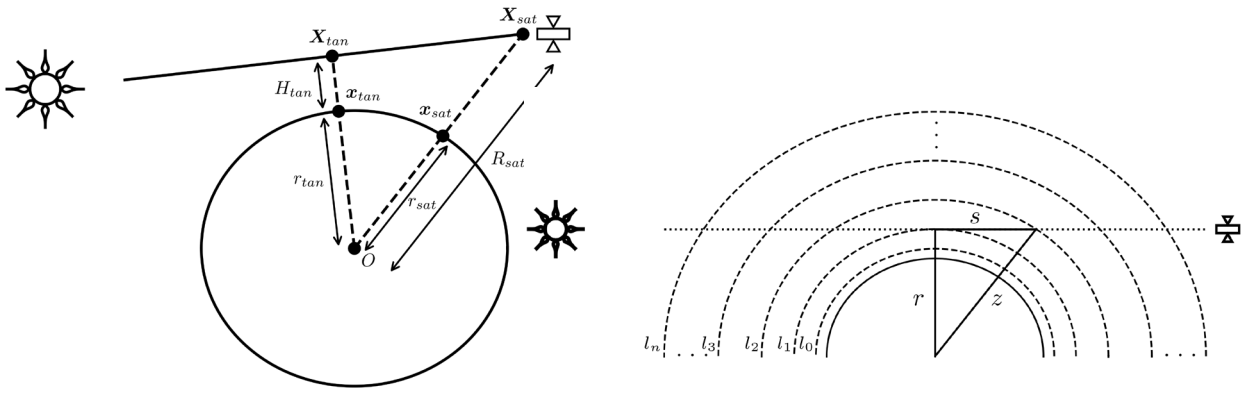

Figure 4. (left) Geometry of an occultation observation. (right) The geometry of the inversion procedure with observationally defined atmospheric layers, l_n. $\boldsymbol{r}$ is the distance from the centre of Mars to the tangent point of the LoS, $\boldsymbol{z}$ is the distance from the centre of Mars to each successive layer and $\boldsymbol{z}$ is half the path length through that and all internal layers.

The geometry parameters recorded in each observation specify the height of TGO above the centre of the planet R_{sat}, together with the planetocentric latitude θ_{sat} and longitude ϕ_{sat} of the TGO position. They also give the height H_{tan} of the tangent point above the MGM1025 areoid (Lemoine et al., 2001), defining the term 'altitude' used throughout this paper.

It is useful to define a cartesian coordinate system with origin at the centre of the planet, the positive x axis cutting the 0° meridian, and the positive z axis passing through the north pole. Then, using the geometry of the ellipsoid, it is possible to calculate the cartesian coordinates $\mathbf{x}_{sat} = [x_{sat}, y_{sat}, z_{sat}]$ of the point on the ellipsoid corresponding to the position $(\theta_{sat}, \phi_{sat})$. This is done by first calculating the corresponding radial distance r_{sat} of the point from the centre of the ellipsoid

$$
\begin{aligned}
r_{sat} &= \sqrt{\left[\left(\frac{\cos(\theta_{sat})}{a}\right)^2 + \left(\frac{\sin(\theta_{sat})}{c}\right)^2\right]^{-1}}, \\
x_{sat} &= r_{sat}\cos(\theta_{sat})\cos(\phi_{sat}), \\
y_{sat} &= r_{sat}\cos\theta_{sat}\sin\phi_{sat}, \\
z_{sat} &= r_{sat}\sin\theta_{sat}.
\end{aligned}
$$

Since $\mathbf{x}_{sat}$ is collinear with the centre of the planet and the location of the satellite $\mathbf{X}_{sat}$, a simple rescaling then gives the cartesian coordinates of the satellite location

$$\mathbf{X}_{sat} = \frac{R_{sat}}{r_{sat}}\mathbf{x}_{sat}.$$

Similarly, it is possible to calculate the cartesian coordinates $\mathbf{X}_{tan}$ of the tangent height point, by rescaling the cartesian coordinates of the point $\mathbf{x}_{tan}$ on the ellipsoid corresponding to the position $(\theta_{tan}, \phi_{tan})$. The procedure is as described above for the case of $\mathbf{X}_{sat}$, except that the final rescaling is given as follows

$$\mathbf{X}_{tan} = \frac{r_{tan} + H_{tan}}{r_{tan}} \mathbf{x}_{tan}.$$

Once the cartesian coordinates of $\mathbf{X}_{sat}$ and $\mathbf{X}_{tan}$ are known, the LoS points are readily calculated as points that lie along the line joining $\mathbf{X}_{sat}$ and $\mathbf{X}_{tan}$. To perform the spectral fitting (described in the next section), initial estimates of aerosol opacity and ozone abundance along the LoS points are determined. These initial estimates are not strictly needed to perform the initial opacity retrieval, but are used for subsequent mixing ratio calculations, and were therefore used as initial estimates to optimise the fitting process since they were available. These values were extracted from outputs of the Open University (OU) modelling group Mars GCM coupled to the Analysis Correction assimilation scheme that has a strong heritage in data assimilation on Mars (Holmes et al. 2018, 2019, 2020, Lewis et al. 2005, 2007, Montabone et al., 2006, 2014, Streeter et al. 2020). The GCM is comprised of physical parameterisations (Forget et al. 1999) and a photochemical module (Lefèvre et al., 2004, 2008) shared with the Laboratoire de Météorologie Dynamique (LMD) modelling group, alongside a spectral dynamical core and semi-Lagrangian advection scheme (Newman et al., 2002). It includes the latest sub-models to provide the most realistic modelling of the turbulent processes in the planetary boundary layer (Colaïtis et al., 2013), and a water-ice cloud microphysics package (Navarro et al., 2014) that includes radiatively active water ice clouds and supersaturation. The OU modelling group GCM has been developed in a collaboration between the Open University, the LMD, the University of Oxford and the Instituto de Astrofisica de Andalucia. Initial O_3 values originate from a model run that assimilated O_3 column data measured by the SPICAM instrument during MY 27 (Holmes et al 2018). Although this model run is for a different year, it produces a good initial estimate of ozone for the beginning of the model run assuming that the seasonal O_3 distribution is repeatable from year to year. For temperature, dust and aerosol fields, a different model run was used, that assimilated contemporaneous temperature profiles and column dust data measured by the Mars Climate Sounder (MCS) instrument (Streeter et al. 2020).

3.1.2 Cross-sections

The three primary absorption features acting on the observed atmospheric transmissions in the observational wavelength region between 200 and 650 nm are those due to carbon dioxide (CO_2), aerosols and O_3. Only the cross-section of O_3 is of relevance in this study since wavelengths close to CO_2 absorption are not considered, and the O_3 cross-section values of Malicet et al. (1995) are used here. The spectral absorption characteristics of aerosols exhibit an approximately homogeneous attenuation on the transmission spectra so an increase in aerosol abundance can in principle be modelled as a fit to any part of the spectra well separated from the reserved O_3 band. Due to the spectral shape changes at longer wavelengths due to aerosol particle size these wavelengths are avoided for modelling the aerosol content in the spectra.

3.1.3 Spectral fitting

A least-squares (χ^2) procedure involving minimizing the sum of the squares of the residual differences between the measured transmissions and a best fit model across a range of

wavelengths, is performed utilising the Levenberg-Marquardt algorithm to obtain the best fit solution. Modelled values for aerosol opacity and ozone abundance are extracted for each LoS from the assimilated data set described earlier as *a priori* values for the iterative fitting process, purely to reduce the number of iterations required.

The first iteration of the fitting is performed in the region between 320–360 nm (i.e. outside the O_3 absorption band) for the aerosol abundance determination (Clancy et al. 2016). All parameters in the model were initially fixed except for the aerosol abundance and Angstrom coefficient, which were treated as free parameters over each iteration to determine an aerosol abundance on convergence. The fitting procedure for O_3 abundance then follows, with updated aerosol values, within the wavelength range 240–320 nm on the positive gradient of the O_3 Hartley band. This wavelength range was used since it permits an accurate representation of O_3 abundance based on a measure of the depth of this feature in the spectrum, whilst avoiding the less well characterised transmission values below 240 nm, where there is greater noise in the spectra and straylight contamination represented by a growth in relative errors.

This optimal wavelength range over which to perform the O_3 fit coincides with the magnesium II h and k doublet solar emission at 280 nm, which is often used as a diagnostic of solar activity (e.g. Snow et al. 2019). As the determination of the Hartley band depth in any given spectrum may be influenced by the residual presence of this feature as the LoS moves across the solar disk, the values at 280 nm are discarded and an interpolation is performed either side of this wavelength.

An example of the fitting procedure results on an example spectrum is shown in Figure 3 where the two fits have been combined to construct the final modelled transmission. The model deviates from the observation below 255 nm primarily due to known stray-light within the system causing an excess in the recorded transmission values below this threshold. In general, the results <240 nm are not considered here due to the loss in responsivity of the CCD at these wavelengths (Patel et al. 2017). A lower altitude cut-off is applied to all profiles at the 1% transmission level at a wavelength of 255 nm, below which the signal on the CCD detector becomes comparable to the noise. Using the total abundance extracted from the O_3 fit of the modelled spectra coupled with the cross-section values the total integrated number density (slant density) is then calculated by applying the Beer-Lambert law defined in section 2.3.

3.2 Vertical Inversion

The slant density of an absorbing species gives a measure of the total integrated number of molecules per unit area along the LoS of each measurement. To convert this slant density profile into an associated set of local densities, or a true vertical profile, a vertical inversion of the slant densities is performed.

To achieve this inversion a standard onion peeling process is used (Auvinen 2002, Quemerais 2006, Rodgers 2000), a procedure that requires the observed two-dimensional atmospheric slice be split into concentric layers. This structure, illustrated in Figure 4, is provided by the observational data, each layer being defined by the tangent altitude of the LoS in successive measurements above the same areoid surface defined in section 3.1. This results in a single measured transmission spectrum corresponding to each atmospheric layer. A spherically symmetric atmosphere is assumed in the plane defined by the observed lines of sight. The separate

path lengths that every measurement's LoS takes through each of the atmospheric layers are then calculated geometrically

$$S = \sqrt{z^2 - r_i^2}$$

In combination with an interpolation between the layers, an Abel integral provides the coefficients of the individual elements of the weighting function matrix, **A,** which defines all combinations of path lengths per layer in the two-dimensional observational grid

$$A_{ij} = \int_{z_{min,j}}^{z_{max,j}} f\,(z) \frac{z}{\sqrt{z^2 - r_i^2}} dz$$

Where f(z) is the interpolated pressure as a function of altitude z, $z_{min,j}$ and $z_{max,j}$ are the altitude limits covered by the j^{th} layer. All (virtual) path lengths constructed via this method that are external to the atmosphere will not contribute to the total observed abundance in any given atmospheric line-of-sight and therefore are given a zero weighting in the final matrix.

With the weighted path lengths encoded in the matrix **A** the local densities, **D**, forming the vertical profile can be calculated from the known slant densities, **N**, and their associated uncertainties, ϵ, by a matrix inversion of the form

$$\mathbf{D} = \mathbf{N} \cdot \mathbf{A^{-1}} + \epsilon$$

This then provides a final vertical profile from the observed slant densities. An example of a calculated O_3 vertical profile obtained through this method and its associated slant density profile are shown in Figure 5. Measured O_3 number densities range from ~10^{10} in the lower altitudes down to ~10^6 where the noise floor inherent in the retrieved slant densities is reached.

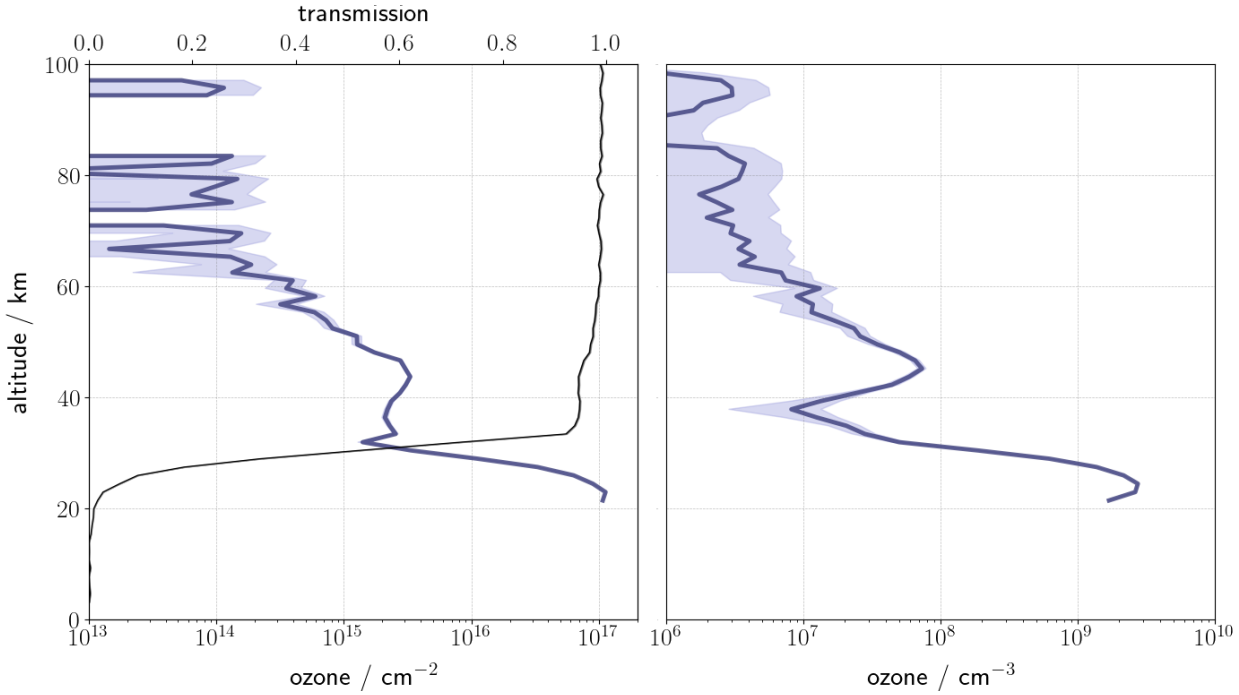

Figure 5. (left) O_3 slant number density (blue) and atmospheric transmission (black); (right) subsequent derived O_3 vertical profile showing the variation in abundance between 100 and ~20 km. This profile corresponds to observation file 20190416_232929, at L_S = 12° in MY35 and a latitude of 74°S.

3.2.1 Uncertainties on the vertical profile

The main source of uncertainty in the occultation data arises from instrumental noise – each spectrum has an associated instrumental error value, with the median value of this error within each occultation being less than 1%.

To determine the associated uncertainty in the retrieval, the 1-σ experimental uncertainty from the random instrumental noise associated with every observed transmission, ϵ, is used in order to calculate a weighted deviation (W) between the model, as evaluated from the Beer-Lambert equation (section 2.3), the fitted model data $M(\lambda)$, and the observation data $\mathbf{x}(\lambda)$.

$$W = \frac{M(\lambda) - \mathbf{x}(\lambda)}{\epsilon}$$

The square of these weighted residuals are the χ^2 values that, through successive iterations, are minimized in order to arrive at a final best fit solution to the modelled data, the associated cost function can be expressed as

$$\boldsymbol{V} = \mathbf{A}^T\mathbf{C}^{-1}\mathbf{A}$$

The covariance matrix, $\mathbf{C}$, in this process describes the covariance of every combination of pairs of measurements, the diagonal elements therefore represent the self-covariance (the variance) of each observation with itself, the individual errors on the obtained slant density measurements

are thus obtained from the square-root of the diagonal of the covariance matrix. An averaging kernel, **K**, is constructed from the weighting function and covariance matrices, whose i_{th} row describes the weighting influence of each atmospheric layer on the i^{th} LoS derived number density:

$$\mathbf{K} = (\boldsymbol{V} + \lambda_s \mathbf{L}^T \mathbf{L})^{-1} (\mathbf{A}^T \mathbf{C}^{-1})$$

Where the matrix **L**, whose contribution is governed by the smoothness coefficient λ_s, is given by:

$$\boldsymbol{L} = \frac{1}{h^2} \begin{bmatrix} -1 & 1 & 0 & 0 & \cdots & 0 \\ 1 & -2 & 1 & 0 & \cdots & 0 \\ 0 & 1 & -2 & 1 & \cdots & 0 \\ \vdots & \vdots & \vdots & \vdots & \ddots & \vdots \\ 0 & \cdots & 0 & 1 & -2 & 1 \\ 0 & \cdots & 0 & 0 & 1 & -1 \end{bmatrix}$$

This kernel represents the quality of the retrieval per retrieved number density value in the final vertical profile.

The uncertainty in the number densities of the final vertical profile is derived in an analogous way to the number densities themselves, Equation 1. In an iterative procedure, the respective errors of each observed slant density are combined in quadrature with the sum of the previously calculated errors on all higher layers, weighted by the proportional path length that those layers represent in the current line of sight column.

$$\partial n_i = \sqrt{\frac{\left(\delta F_i / 2\right)^2 + \sum_{j=0}^{i-1} \left[\delta n_j^2 \cdot dx_j^2\right]}{dx_i^2}} \qquad \text{Equation 1}$$

This quantity is then scaled based on the path length of the layer in question (the lowest layer) in the current column to obtain a final error on the number density in that layer of the vertical profile.

4 Results and discussion

4.1 O_3 vertical distribution

Figure 6 shows the seasonal variation of the O_3 vertical profiles from the NOMAD-UVIS retrievals for observations made in the northern hemisphere and the southern hemisphere. Generally, retrieved NOMAD O_3 profiles extend to 50-60 km altitudes, based on NOMAD O_3 sensitivity limits and Mars upper level O_3 abundances (previous section, e.g., Figure 5). It should also be noted that these plots show the vertical profile over varying latitudes – in some cases, moving from the polar regions to equator in a small L_S period. Thus, care must be taken in interpreting these plots, as latitudinal gradients can appear mapped into temporal (L_S) changes.

Given the strong photochemical anticorrelation of O_3 with H_2O, we also present the water profiles simultaneously retrieved with the IR channel of NOMAD (Aoki et al. 2019), providing the first direct comparison of contemporaneous and co-located O_3 and H_2O vertical profiles. Unfortunately, at the time of writing NOMAD water profiles retrievals are only publicly available

up to L_S = 345° in MY34 (Feb 2019), and therefore the water profiles shown in Figure 6 only contain NOMAD water retrievals to L_S = 345°.

To provide a comparative water vapour dataset for the remaining period through to L_S = 320° in MY35 (November 2020), we performed an assimilation of MCS v5.3.2 temperature profiles and column dust retrievals (Kleinböhl et al. 2017) using the OU modelling group Mars GCM described in section 3.1.1. An ensemble of assimilation runs was conducted over the whole time period, in which the parameters of albedo and thermal inertia of perennial surface ice were varied to select an optimum water vapour simulation. Navarro et al. (2014) adopted this approach in a forward GCM study, to model Mars atmospheric water column variations. The selected assimilation run was chosen to optimize water vapour comparisons with respect to NOMAD water vapour retrievals towards the end of the period for which they are available (late 2018, when the MY34 dust storm effects have largely abated). Comparison with as yet unpublished NOMAD water profile observations for this period show the modelled water to be qualitatively consistent with the observed water profiles (S. Aoki, *pers. comm.*)

The bottom panels of Figure 6 present this NOMAD-model composite description of water profiles corresponding (in position and L_S) to retrieved NOMAD O_3 profiles in the top panels. This provides a partial comparison of NOMAD water vapour and O_3 profile measurements, for the published dust storm period of NOMAD observations (L_S = 190-345 in MY34). It also allows a predictive (model) description of the very distinct behaviour of Mars water vapour centred on the aphelion climate of Mars (L_S ~0-180) in MY35.

NOMAD-retrieved O_3 profiles are presented in the top panels of Figure 6 and compared to simulated O_3 profiles in the middle panels. These simulated O_3 profiles are strictly based on the MCS temperature and dust assimilation modelling described above. Consequently, they correspond to modelled, not observed, atmospheric water vapour distributions for the entire presented L_S range in Figure 6. These simulated water vapour profiles are constrained by assimilated MCS temperature and dust profiles, as described above, such that they more closely correspond to contemporaneous water vapour saturation conditions, including the MY34 dust storm, high latitudes, and the aphelion period.

Nevertheless, the model-NOMAD comparisons for O_3 profiles in the top two panels of Figure 6 still retain significant uncertainties associated with GCM simulations of Mars water vapor (Navarro et al., 2014; Daerden et al., 2019). Direct assimilation of NOMAD retrieved H_2O profiles should allow much more quantitatively direct (and photochemically diagnostic) comparisons of model and observed O_3 profiles. For current purposes, these model/data O_3 comparisons allow a preliminary assessment of the detailed seasonal and spatial variations of the vertical distribution of Mars O_3 from NOMAD, in the context of a best-effort approach for modelling Mars atmospheric water profile behaviour based on assimilated dust and temperature profiles.

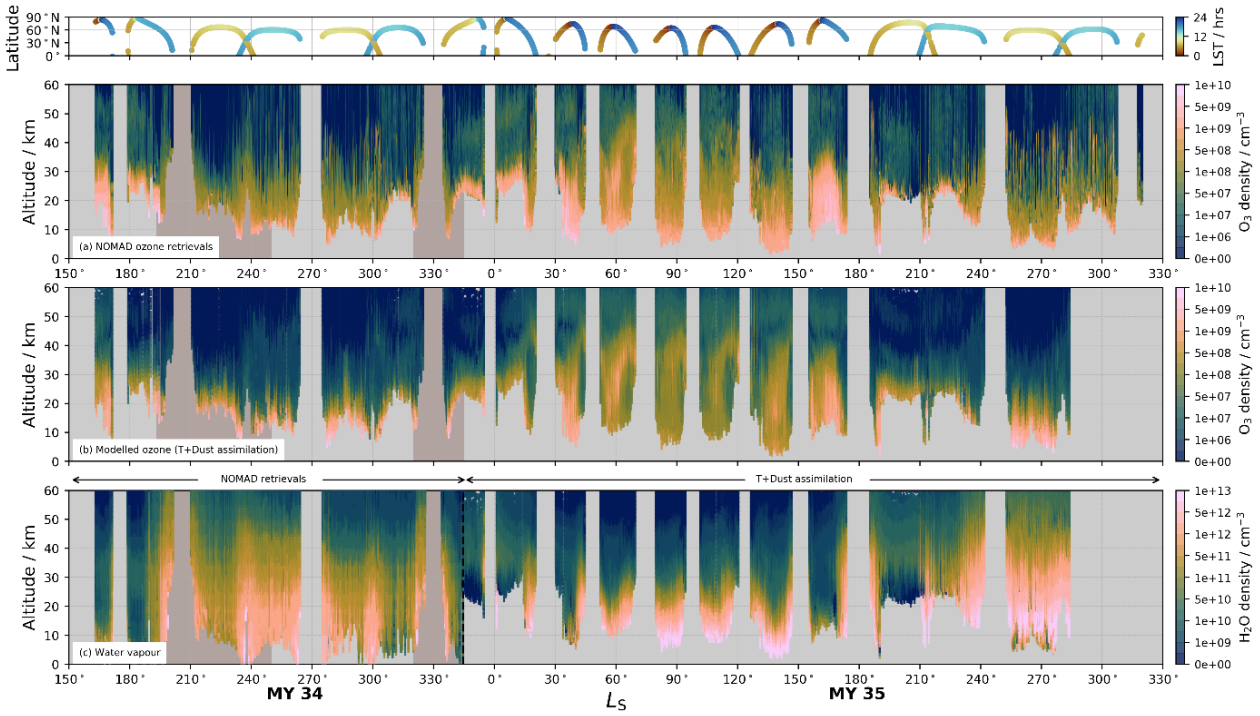

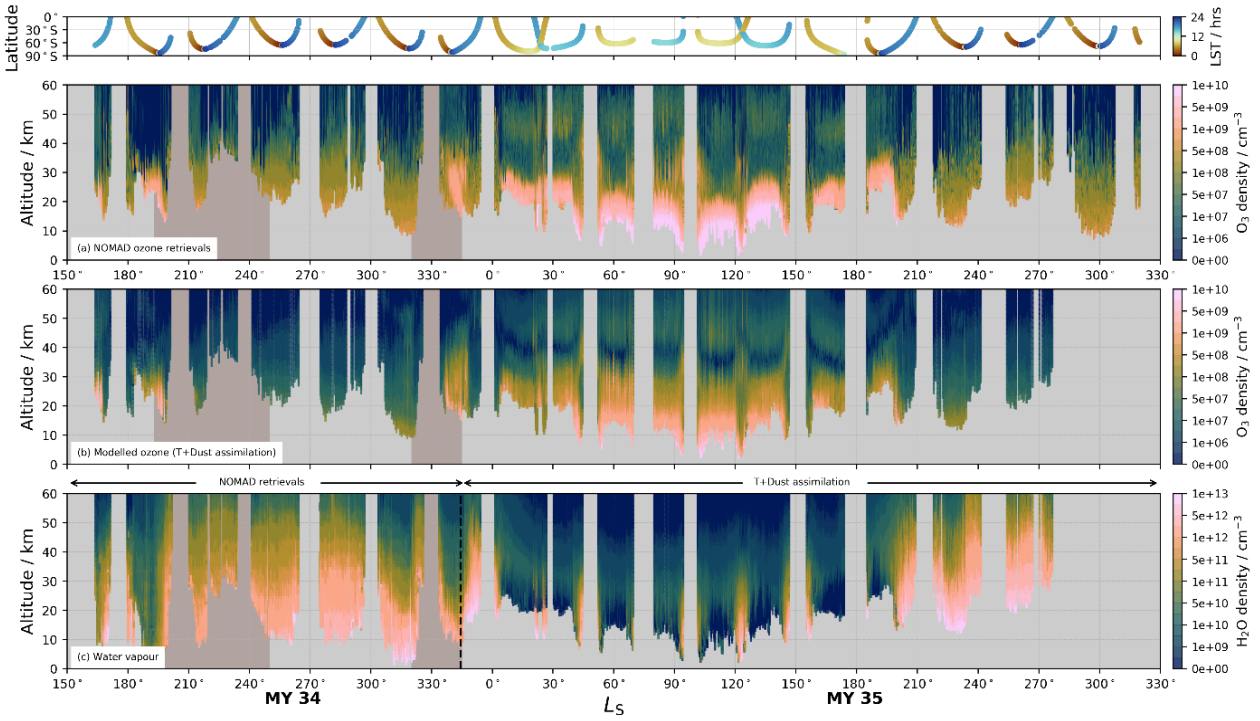

Figure 6. (top) Northern hemisphere altitude profiles for (a) NOMAD retrievals of O_3; (b) modelled O_3 based on initial conditions derived from SPICAM observations and evolved through time considering assimilated temperature and dust observations from MCS; (c) retrieved and modelled H_2O abundances. NOMAD retrievals of H_2O are from Aoki et al. (2019). **(bottom)** The

equivalent as above, but for the southern hemisphere. The UVIS O_3 retrieval profiles cover the period L_S = 163° in MY34 to L_S = 320° in MY35 and consist of 5990 individual profiles and 677,473 individual spectra. The wide and narrow shaded periods represent the timing of the MY34 global dust storm and regional storm respectively. Altitude values are with reference to the Mars areoid, and the latitude that each profile is taken at is indicated by the top plot.

The effect of the MY34 global dust storm (approximately L_S = 190 – 250°) on the O_3 retrievals, through reduced limb transmission, is most noticeable in the increasing lower altitude cut-off due to the sharp increases in dust loading (e.g. Smith 2019; Liuzzi et al. 2020; Montabone et al. 2020). In the equatorial and mid-latitudes, retrievals are only possible down to ~30 km, allowing only mid-to-upper level regions of atmospheric O_3 to be detected. At higher latitudes, where lower dust content is present, O_3 retrievals are possible to altitudes below 10-20 km. Elevated water abundances at high altitudes (>30-50 km) are observed in both northern and southern hemispheres during the MY34 (2018) global dust storm after L_S = 190-200° (Aoki et al. 2019, Fedorova et al. 2020), similar to behaviour observed and modelled during the MY28 (2007) global dust storm (Heavens et al. 2018). This leads to correspondingly reduced O_3 abundances above 30-50 km, associated with the strong photochemical anti-correlation between the two species. A comparison of the difference in MY34/35 O_3 distribution during the global dust storm period is given in section 4.2; however, care must be taken when comparing periods in Figure 6, since the latitude of the observations vary significantly and will be different between Mars years.

Altitude-resolved NOMAD O_3 abundances below 15 km altitudes represent new measurements and will prove significant in assessing previous column (nadir) measurements of Mars ozone (e.g., Perrier et al., 2006). Such column measurements are often dominated by maximum lower atmospheric O_3 abundances, particularly at high latitudes, that may contribute disproportionately to existing model-data disagreements for column O_3 comparisons (Clancy et al., 2016). Peak near-surface O_3 densities (and mixing ratios) are generally observed to be present throughout the Mars year and occur, in part, due to reduced HO_x production from H_2O UV photolysis (associated with increasing CO_2 extinction of UV radiation, e.g., Montmessin and Lefèvre, 2013).

This near-surface O_3 layer is particularly evident at southern winter latitudes, when cold aphelion temperatures lead to the aphelion cloud belt (ACB) and much reduced transport of water vapor into the southern winter hemisphere (Clancy et al., 1996), and thus minimum HO_x loss rates for O_3 at all altitudes (Lefèvre et al., 2004; Daerden et al., 2019). Figure 6 demonstrates this behaviour in, respectively, NOMAD retrievals and assimilation modelling of O_3 and H_2O abundances in the southern hemisphere lower atmosphere (L_S = ~0-180°). The northern hemisphere winter is generally obscured due to the presence of dust from the MY34 global dust storm. Increasing O_3 abundances below ~15 km altitudes are retrieved between L_S = 190 – 250°, associated with northern winter. But overall, reduced O_3 and increased H_2O abundances (both, in this case, from NOMAD retrievals) are present relative to the aphelion, southern winter period.

Figure 6 also indicates distinct high altitude (~50 km) O_3 maxima that extend over high latitudes, at ~60-90° north and south latitudes, but most prominently in the south. These high altitude, high latitude peaks for O_3 abundances likely reflect sharply decreasing H_2O abundances with altitude at these locations and times (e.g., see Figure 10). However, SPICAM identified similarly high altitude O_3 peaks during southern winter polar night (Montmessin and Lefèvre, 2013), which they associated with upper level, meridional transport of O. A similar process creates winter (N and S) and equinoctial peaks in O_2 (1.27 μm) polar nightglow (Clancy et al., 2012). Both

behaviours were modelled in these previous studies as restricted to latitudes above 70°, and associated with upper level, transport-enriched O abundances. It is possible this behaviour extends to lower latitudes and contributes to the NOMAD observed O_3 peak abundances at similar altitudes (see next section).

The high latitude, high altitude peak O_3 abundances retrieved by NOMAD solar occultations are at the sunlit (sunrise and sunset) terminators. It is apparent at high latitudes in both hemispheres over the aphelion period but is most prominent in the southern hemisphere. In the southern hemisphere, a distinct enhanced region of O_3 is observed at an altitude of about 50 km, beginning at L_S ~ 10° and at a latitude of approximately 60°S. This enhancement varies in abundance over latitude but persists from L_S ~10 through to L_S ~200° in the southern hemisphere.

Figure 7 shows the ratio of the O_3 abundance observed by NOMAD, to that simulated by the GCM following assimilation of MCS dust and temperature observations. There is good agreement between the model data and retrieved values during perihelion at varying high and low altitudes in the northern hemisphere, with a similar trend in the southern hemisphere at high altitudes. At aphelion, there is a wider spread of O_3 underestimation in altitude and L_S in both north and south hemispheres, but with a lower observation/model ratio value indicating a better agreement relative to perihelion. During this time, a band of approximately unity ratio is present at an altitude of ~30-40 km in both hemispheres.

Figure 6 showed that the qualitative distribution of O_3, including the structure and timing of the high latitude, high altitude peaks, is represented well by the GCM. However, Figure 7 shows that, in general, the absolute abundances simulated in the GCM are over a factor of ten lower than that observed by NOMAD. This is most likely due to the fact that the water saturation conditions are only partially constrained by the temperature and dust assimilation, such that water abundances are not adequately represented in the model simulations. Model assimilation of the observed NOMAD water profiles, once publicly available, will address this modelled O_3 abundance deficiency.

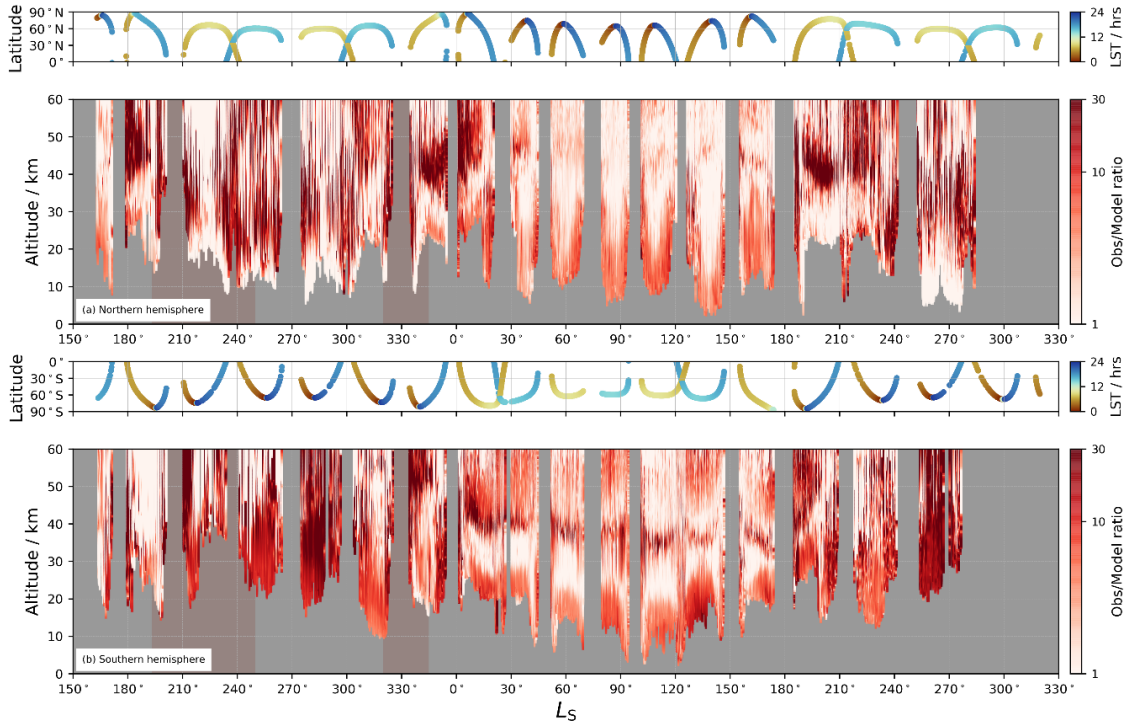

Figure 7. Ratio of the observed to modelled ozone abundance shown in Figure 6 for (a) the northern hemisphere and (b) the southern hemisphere. Lighter (darker) shading indicates stronger (weaker) agreement between observation and model abundances; higher ratio values indicate that modelled values are lower than that observed by NOMAD.

4.2 Latitudinal distribution

Figure 8 shows the NOMAD ozone profile retrievals, plotted as a function of latitude for L_S bins of 20°. Towards perihelion (L_S = 251°) in northern winter, high latitude ozone is generally present at low altitudes, and perhaps comparable to the southern winter (L_S = 90°) equivalent high latitude regions. A comparison of the northern autumnal equinox periods for MY34 and MY35 (L_S = 160-180° and 180-200°) indicates that observed O_3 abundances extend to higher altitudes in the non-global dust storm year (MY35). Presumably, ozone abundances above ~20 km are reduced during the MY34 global dust storm, due to the elevated water abundance above these altitudes associated with this storm (e.g., Aoki et al., 2019). The period L_S = 180-200° presents an especially high number of observations in both years, and thus is most appropriate for this comparison. In MY34 during this period, O_3 reaches an altitude of 20-30 km in the southern polar regions, at the onset of the global dust storm. In the MY35 equivalent period, O_3 reaches an altitude of 30-40 km, highlighting the reduction of O_3 abundances in this region in MY34 associated with dust-driven increases in water vapour. Northern mid-latitudes (~30-45°N) also exhibit higher O_3 abundances in the L_S = 180-200° period in MY35 with respect to MY34, but limited observations during the MY34 period make it difficult to compare this latitude region further.

Following the annual global dust activity increase centred near L_S = 330° (e.g., Smith, 2004; Kass et al., 2016), the development of increased O_3 abundances to altitudes of ~35 km is observed in the southern polar regions at L_S = 340 – 350°), as the equinoctial precursor of the southern winter polar peak in O_3. The previously mentioned high altitude peaks in the north and south high latitudes also start to become more clearly visible at this time.

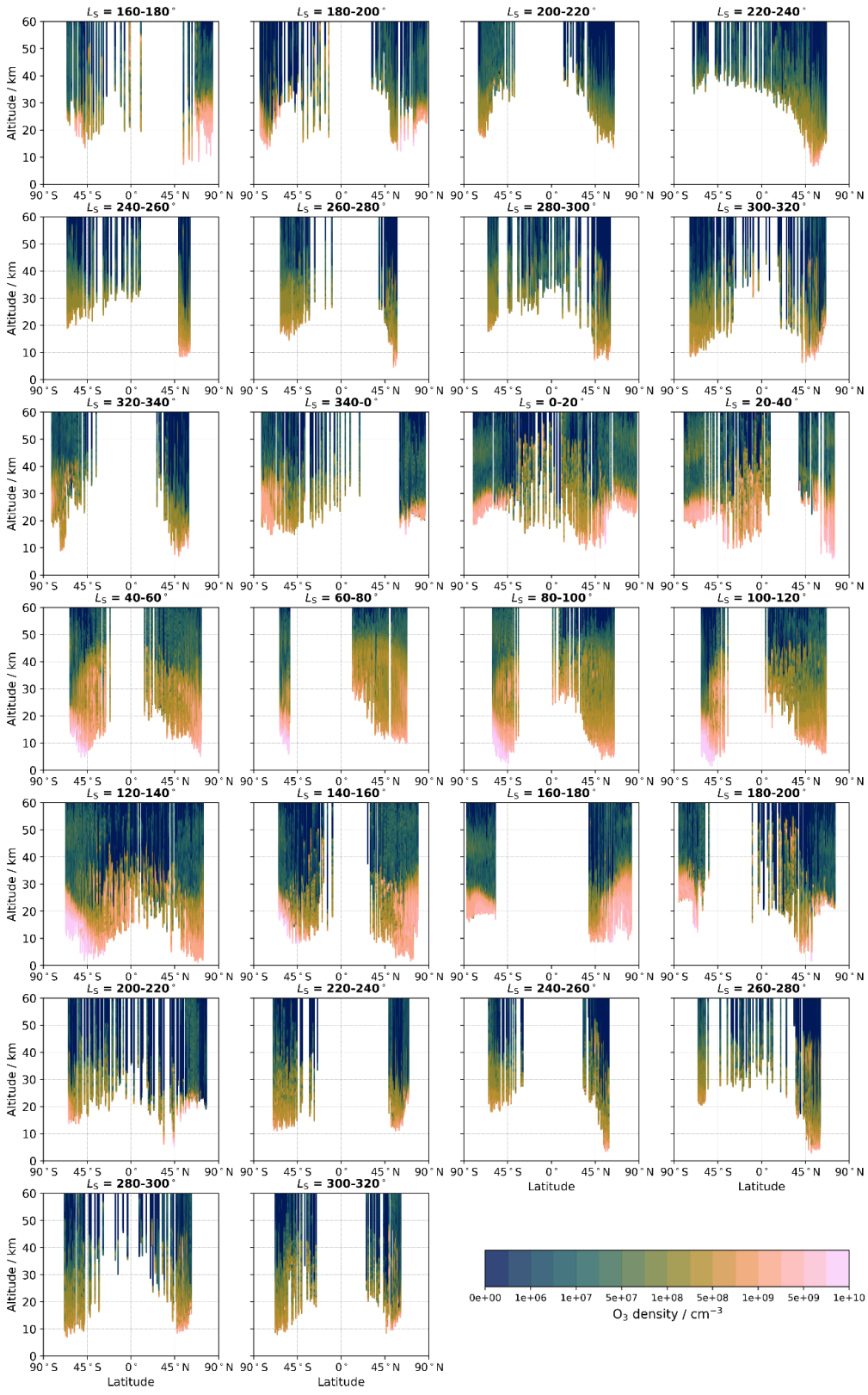

Figure 8. Latitudinal distribution of the NOMAD O_3 retrievals over 1 martian year. Each plot shows the vertical profiles obtained during a $Ls = 20°$ period.

The first occurrence of a high-altitude enhancement appears in the northern polar regions at L_S ~ 345°, at an altitude of ~45 km. It develops over a latitude range of 60 – 90°N, and persists through to L_S ~ 40°, extending over an altitude range of 45 – 55 km. Towards northern summer, the high-altitude peak merges with general increases in low-to-mid latitude O_3 above 20 km altitudes. However, a 45°N latitude minimum in this behaviour appears centred on L_S = 60-100°, which corresponds to a minimum in O_3 columns observed at that time (Perrier et al., 2006; Clancy et al., 2016). The notable low-to-mid latitude increases in 20- 50 km altitude O_3 over the extended northern summer season (L_S = 40-120°) reflect the aphelion saturation conditions for water vapor above ~20 km altitudes. This orbitally-driven cooling of the global Mars atmosphere leads to the formation of the ACB (Clancy et al., 1996; Smith et al., 2004; Montmessin et al., 2004) and sharp increases in O_3 abundances above 20 km (Clancy and Nair, 1996; Lefèvre et al., 2004) at this time. These vertically extended increases in aphelion O_3 abundances continue until L_S ~120°, after which O_3 abundances above 20-30 km begin to decrease with increasing atmospheric temperatures and water vapor. The ACB similarly declines over this period (Smith et al., 2004).

The high-altitude enhancement in the southern high latitude region appears in the L_S = 0-20° period, at an altitude of 40-50 km and latitudes > 55°S. This peak is observed at latitudes >55°S through to L_S = 20-40°, growing in abundance and altitude (40-55 km). A lack of observations at high southern latitudes until L_S = 120-140° means that the latitudinal extent of this enhancement throughout this period cannot be confirmed, but the southern latitudinal margin of the enhancement is observed in the L_S = 40-100° period, at a latitude of 55°S. The southern high-altitude enhancement is observed next at L_S = 120-140°, and subsequently observed through to L_S = 160-180°.

At L_S = 40-60° in Figure 8, meridional circulation is evident in the latitudinal O_3 distribution. O_3 formation along the flow paths of O atoms highlights the meridional circulation, in this case during the transition from equinoctial to solstitial circulation. The downwelling branch of the main Hadley cell typical of this time of year (e.g. Barnes et al. 2017) shapes the O_3 distribution in the southern hemisphere, between 50–20 km, with evidence of the thermally indirect cell at high northern latitudes at altitudes between 20–40 km. Progressing towards solstitial circulation, in the L_S = 60–80° period there is a possible signature of a thermally indirect cell, spanning a latitude range of ~65°N to 10°N and an altitude of 20–40 km, respectively. It should be noted that the meridional circulations highlighted here do not represent the strength or extent of the circulation nor the transport of O_3, but serve only to highlight the (possibly weak) circulation paths where the formation of sufficient O_3 is permitted and thus made observable.

The newly identified high altitude O_3 enhancements show a distinct symmetry in the period L_S = 0-20°, with a weaker symmetry at the autumnal equinox (L_S = 160-180°). The high altitude enhancements in both northern and southern 60-90° latitude ranges are observed to form during the vernal equinox period and are not restricted to the southern polar night as previously observed. At L_S = 160-180°, the southern high altitude enhancement is comparable in abundance to that at the vernal equinox, with the northern high-altitude peak being significantly lower in abundance, but confined to a slightly higher altitude (55 km) than its vernal equinox counterpart. In general, we find the high altitude O_3 enhancement forms during the equinoctial periods, with northern polar high altitude peaks showing a maximum at vernal equinox, and the southern peak persisting for a much longer period between vernal and autumnal equinox.

The transport-induced formation mechanism for the high altitude polar night layer observed by Montmessin and Lefèvre (2013) could potentially be a contributing factor to (but not

solely responsible for) the formation of the high latitude high altitude enhancements observed by NOMAD during both equinoxes. Montmessin and Lefèvre (2013) described the formation of the polar night high altitude layers via the transport of odd O-rich air (created through CO_2 photolysis) from low latitude regions into both north and southern high latitude regions. During the periods of observed high altitude O_3 enhancement by NOMAD, transport of O and H to both poles is expected to take place through the equinoctial equator-to-pole circulation, potentially contributing to the pattern of occurrence of O_3 at high altitudes in both hemispheres.

Figure 9 shows the modelled zonal cross-section of O and H atoms at 0500 local time (similar to the 'sunrise' times of the NOMAD occultation measurements during that period) and based on the MCS dust and temperature assimilation between L_S = 0–20°.

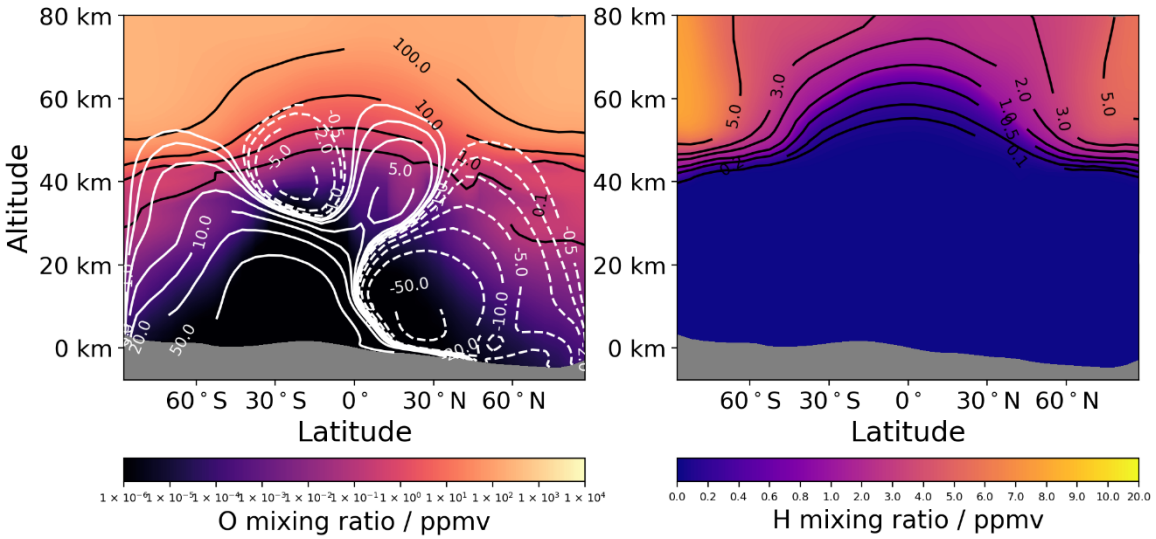

Figure 9 Zonal plot of meridional flow of O (left) and H (right) atoms at a local solar time of 0500 between L_S = 0 – 20° MY35, from the assimilation of dust and temperatures from MCS. Black contours indicate abundance of O and H respectively in ppmv, solid (dashed) white contours display the anti-clockwise (clockwise) mean meridional circulation in 10^8 kg/s.

In the southern hemisphere, at latitudes poleward of 45°S the O atom flow descends to an altitude of ~20 km. In the northern hemisphere, the O atom abundance begins descending at around 30°N, reaching altitudes as low as ~10 km. In both hemispheres, the H atom flow extends to high latitudes but is confined to altitudes > 40 km. The transport of O and H from the equatorial region to higher latitudes in both hemispheres, in roughly equal proportions, is thus enabled through the equinoctial meridional transport shown in Figure 9. The observed high altitude O_3 enhancements likely exist as a balance between O_3 formation at low altitudes (through recombination of O with oxygen in the absence of H_2O) and destruction of O_3 which regulates the upper altitude limit through reaction with H. Figure 6 reinforces this given that during vernal equinox, the water abundance in both hemispheres is confined to relatively low altitudes (see also Figure 11). It is therefore likely that this coupled effect of anti-correlation with H_2O (enabling the creation of O_3) and the equinoctial transport of H atoms (contributing to the destruction processes at the upper altitudes) results in the vertical 'band' of the enhancement observed. The proportion of either process in creating the observed enhancement is, however, not known, requiring future investigations involving the assimilation of contemporaneous O_3 and H_2O NOMAD observations

as well as wider-scale dust and temperature observations to ensure the best possible reconstruction of the global atmospheric state.

4.3 O_3 distribution compared to H_2O

O_3 and H_2O are always photochemically anti-correlated in terms of HO_x chemistry. It is not, however, the case that when H_2O abundance is relatively high, O_3 abundance will always be relatively low. NOMAD is the first instrument capable of measuring simultaneously O_3 and H_2O vapour profiles to demonstrate this through observations; here we discuss the relationship of the two species regarding their relative vertical distribution.

Figure 10 presents the comparison of O_3 and H_2O as a function of altitude and latitude. Figure 10 shows the distribution of NOMAD O_3 and H_2O retrievals from L_S = 163° onwards for the remainder of MY34, and also the NOMAD O_3 compared to the modelled O_3 (following MCS dust and temperature assimilation) for MY35 up to L_S = 280°.

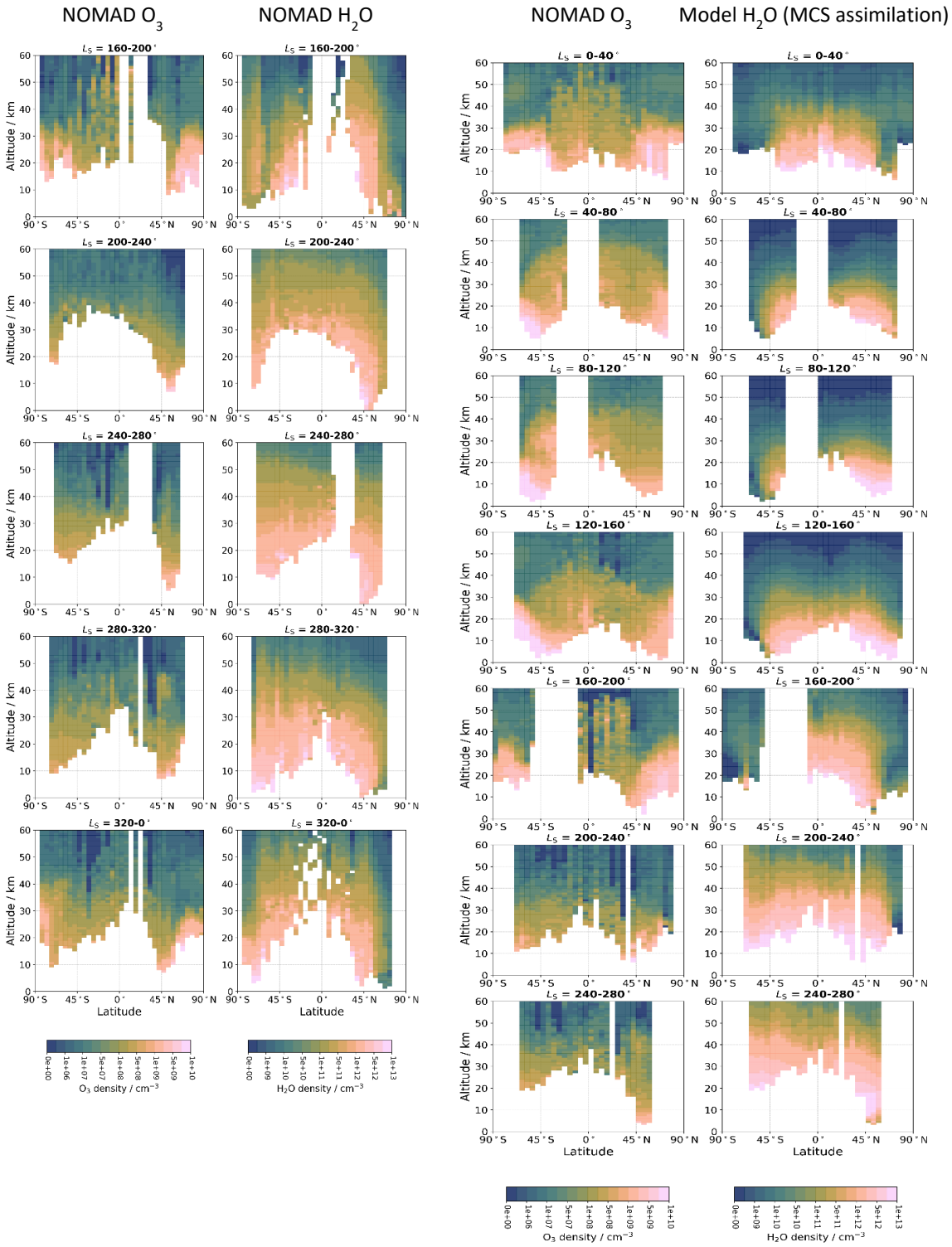

Figure 10. Latitudinal distribution comparison of **(left column pair)** NOMAD O_3 retrievals and (right column) NOMAD H_2O retrievals (Aoki et al. 2019), in L_S intervals of 40° during MY34, and **(right column pair)** as left pair but for MY35. Retrievals are binned every 5° latitude and 1 km altitude for clarity. The same colour scale is used for both species, with different absolute scales.

At perihelion in MY34 between L_S = 160-340° there is a greater relative density of NOMAD-retrieved H_2O, particularly at high altitudes (> 30 km) in both hemispheres, due to the ~20 K increase in average atmospheric temperatures associated with the ~40% increase in solar flux (Clancy et al., 1996), and due to the related intense dust activity during the global and regional storms (Smith 2019; Liuzzi et al., 2020). During this period, O_3 is confined to lower altitudes, with the altitude of peak O_3 values in general being coincident with peak H_2O values. O_3 and H_2O show a similar overall trend in increasing relative abundance with decreasing altitude.

Towards aphelion in MY35 during the northern summer there is an overall lower density of modelled H_2O, and a higher density of O_3, consistent with the generally colder aphelion season due to decreased solar insolation. In MY35, O_3 retrievals were possible to lower altitudes than in MY34 due to the absence of storm-related high dust loading. From L_S = 0-160°, H_2O is confined below 40 km in both hemispheres, showing dry south polar regions to the minimum altitudes observed by NOMAD (~5-10 km). At L_S = 0-40° the high latitude, high altitude enhancement of O_3 at 40-50 km is coincident with low H_2O abundance. In the context of this feature (in both hemispheres), the H_2O density is low below 30 km at latitudes > ±55°, with a higher density region of H_2O present between approximately 30-40 km at southern high latitudes and approximately 30-50 km at northern high latitudes. The vertical onset of the high latitude, high altitude O_3 enhancement correlates with where the H_2O peak begins to decrease, with the O_3 enhancement beginning at an altitude of ~40 km at southern high latitudes, and ~45 km at northern high latitudes. Above this altitude, H_2O density decreases steadily. One possible cause for the upper altitude cut-off of the O_3 enhancement could possibly be the meridional flow of H atoms via equinoctial circulation, shown in Figure 9.

From L_S = 40-120°, O_3 density is consistently high across all latitudes up to altitudes of ~50 km, consistent with the generally low H_2O densities in these regions. At L_S = 120-160° H_2O abundances increase across all latitudes, shifting the abundances upwards by ~5 km in altitude. This general increase in H_2O at high altitudes results in a corresponding decrease in O_3, showing an anti-correlation with the H_2O distribution across latitudes and above 30 km. With the reappearance of the high latitude, high altitude O_3 enhancement >40 km, no corresponding H_2O peak is seen below the O_3 enhancement, as observed during vernal equinox. It is possible that the high latitude, high altitude O_3 enhancement may be influenced more by H_2O at vernal equinox than autumnal equinox due to the transition from warmer perihelion to cooler aphelion, with the influence from meridional circulation of O and H atoms having a weaker/stronger contribution, respectively. Assimilation of NOMAD H_2O retrievals during these periods will provide further insight to this process.

Figure 11 shows a sample comparison of several coincident NOMAD O_3 and H_2O profiles (top row = NOMAD H_2O observations, bottom row = assimilation model profiles). These profiles cover the time period L_S = 199.7° (MY34) to L_S = 165.8° (MY35), at high latitudes (up to 79.6°S and 65°N). In MY34 through perihelion, the relative abundance of both O_3 and H_2O increases strongly towards the surface with peak values of both species occurring at the lowest altitudes, consistent with the build-up of O_3 at lower altitudes due to the reduced photolysis rates arising from the overlying CO_2 atmosphere (Montmessin and Lefèvre, 2013). In MY35 through aphelion, H_2O profiles show an inflection around 20-30 km, resulting in maximum H_2O abundances occurring at higher altitudes than during perihelion. O_3 profiles show a sharp drop at the point of the H_2O maxima. While the photochemical anti-correlation of O_3 and H_2O remains valid throughout the martian year, there is a clear difference in the shape of the H_2O profiles between

the warmer, wetter perihelion season and the colder, drier aphelion season (Clancy et al. 1997), which drives the shape of the O_3 profile below 40 km and contributes to the creation of the high altitude O_3 enhancement. Direct NOMAD O_3-H_2O comparisons in MY35 should confirm these observations in detail. Furthermore, assimilating retrieved NOMAD H_2O profiles will lead to much better O_3 absolute abundance simulations, which appear consistently lower than NOMAD measurements (Figure 7).

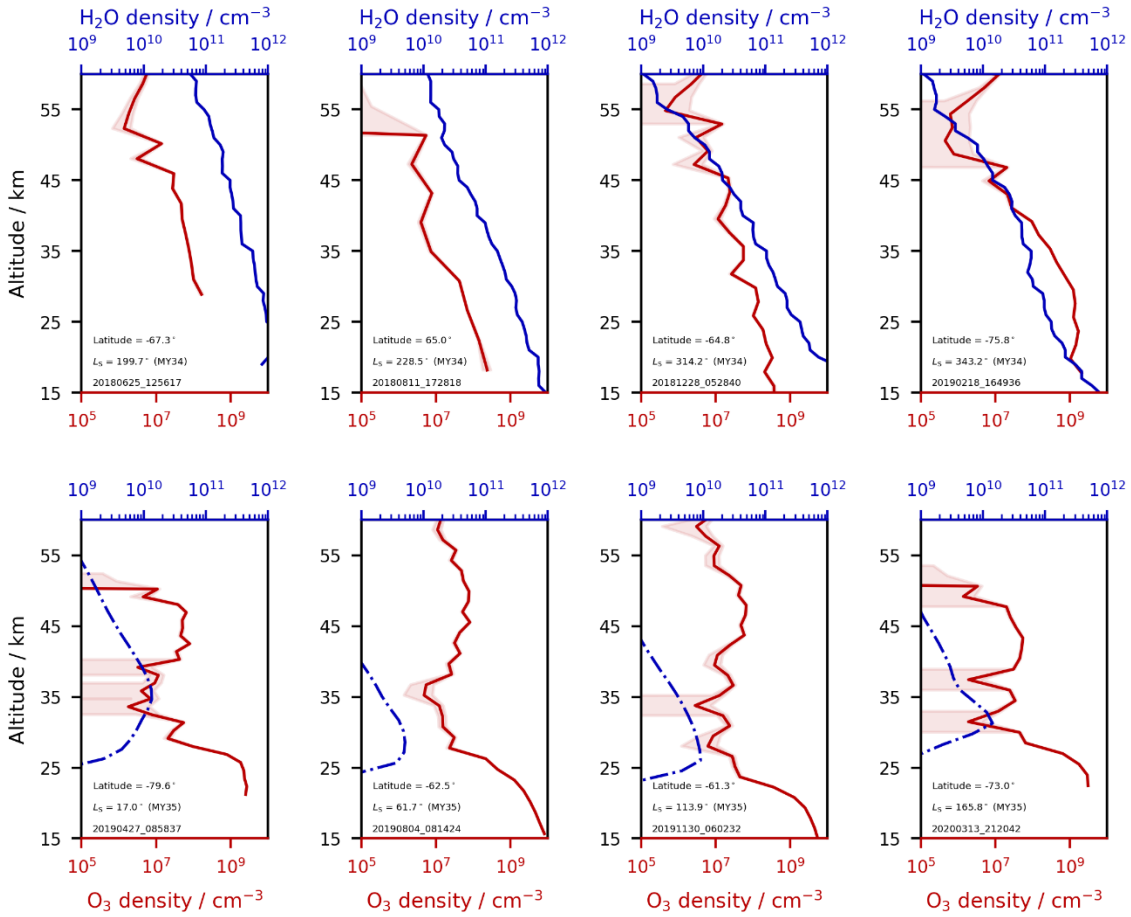

Figure 11. Vertical profiles of O_3 and H_2O. Top row shows a comparison of NOMAD O_3 and NOMAD H_2O retrievals, bottom row shows a comparison of NOMAD O_3 with modelled H_2O from the MCS dust/temperature assimilation. These profiles cover the period L_S = 199.7° MY34 to L_S = 165.8° MY35. The observation data filename, L_S and latitude are shown in each sub-plot.

4.4 Night-to-day and day-to-night terminator perspectives

A key feature of the non-Sun-synchronous orbit of TGO is that it allows NOMAD to observe different local times of day on Mars. This benefit is key to NOMAD nadir observations, which enable total column measurements at varying local times across the planet. Whilst occultation observations are also made at differing local times as a function of latitude and season, by definition an occultation observation always occurs at local sunrise/sunset, at the terminator.

Interpreting fine-scale diurnal variations in NOMAD occultation data should be done with care, since occultation measurements will always be performed with the observation tangent point at the day/night boundary.

It is valid, however, to draw conclusions on the difference between sunrise and sunset occultations. From the perspective of viewing geometry, the TGO spacecraft is in eclipse behind Mars prior to a sunrise occultation; the NOMAD-Sun LoS therefore transects the atmosphere that is emerging from the nightside conditions of Mars for a sunrise occultation. For a sunset occultation, the opposite is true, where TGO points towards the Sun after passing over the dayside of Mars. For a sunset occultation, the NOMAD-Sun LoS therefore transects the atmosphere that has been subjected to the dayside conditions of Mars (high temperatures, solar UV). Both cases will consist of observations with part-night/part-day optical paths, with the difference being the exposure period of each optical path to day/night conditions.

Figure 12 shows the vertical profiles for a group of observations between L_S = 30-60°, and latitude range 30-70°S. Whilst local time is plotted, this serves primarily to discriminate between sunrise and sunset occultations, to discern the differences between the nightside and dayside atmospheric 'context' of the occultations.

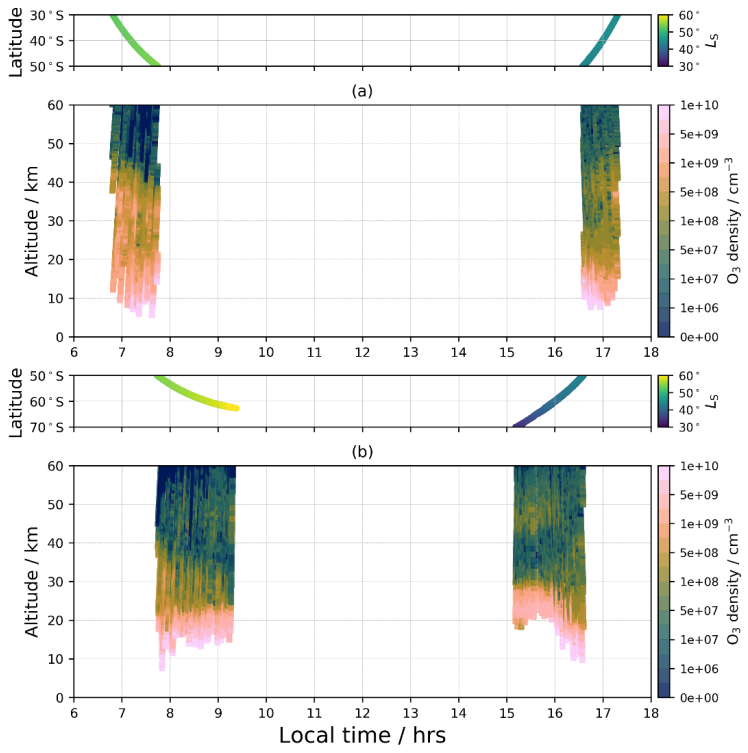

Figure 12. Sunrise and sunset occultations showing the O_3 vertical profile number density, for the period L_S = 30 – 60°. (a) shows the observations for the latitude range 30-50°S, and (b) the observations for 70-50°S. The exact latitude and L_S for each profile is shown above each plot.

In Figure 12a, the sunrise occultations show an O_3 number density at approximately 10^9 cm^{-3} up to an altitude of ~40 km. This is in stark contrast to the equivalent sunset occultations, where the equivalent number density only reaches an altitude of ~20 km. Figure 12a thus shows a clear bias towards higher ozone abundances at greater altitudes than the equivalent sunset

occultations for the equivalent latitude within the same period. This difference likely arises from diurnal partitioning between O_3 and O, which leads to nighttime conversion of O to O_3 when O_3 photolysis is inactive, resulting in significant O_3 increases above 20-30 km altitudes associated with altitude increasing O densities (e.g., Nair et al., 1994). Day-time photolysis of O_3 to O leads to reduced O_3 densities above 20-30 km. Consequently, the photolysis-driven diurnal partitioning of O_3 and O can plausibly create the observed sunrise and sunset O_3 profile variations indicated in Figure 12a. However, the occultation atmospheric paths transect day and night illuminated regions at both terminators, and diurnal O_3 variations associated with O_3 partitioning are not instantaneous at the terminators. Detailed modelling is required to assess these NOMAD sunrise-sunset distinctions, but they should yield new constraints on Mars photochemistry.

Figure 12b shows a similar grouping of sunrise/sunset occultations, in this case for the region containing the high-altitude O_3 peak at ~50 km in the southern high latitudes (50-70°S) in late southern fall (L_S = 60-30°). Here, the O_3 profiles exhibit more complex vertical structures yet less notable differences between the sunrise and sunset occultation data sets. Trends in vertical structure within the sunrise and sunset profile sets may reflect the 15-20° changing latitudes across these observational sequences, which are significant in terms of the polar hood/vortex conditions sampled. Similarly, the change in seasonal coverage between the sunrise (L_S = 30-45°) and sunset (L_S = 45-60°) observations is also significant for these autumnal, high latitude conditions. Thermal tides and planetary waves can also lead to complex local time and longitudinal variations of O_3 at this time as well (Lefèvre et al., 2004).

5 Conclusions

We have analysed the first martian year of occultation observations from the NOMAD instrument on ExoMars TGO and presented a new climatology of the vertical distribution of O_3 for the period L_S = 163° in MY34 to L_S = 320° in MY35. The vertical, latitudinal, and seasonal (L_S) variations of these retrieved NOMAD O_3 profiles are compared with coincident NOMAD H_2O profiles obtained during the MY34 global dust storm (Aoki et al., 2019), and to OU data assimilation modelling of O_3 and H_2O profiles, in which MCS temperature and dust profiles are assimilated to constrain water vapor saturation conditions.

These NOMAD O_3 profile retrievals present the first detailed, global description of Mars O_3 vertical distributions as a function of season and latitude, and with accurate sensitivity from below 10 km (depending on variable atmospheric aerosol extinction) to above 50 km (depending on variable O_3 abundance) altitudes. Key global-scale variations in Mars atmospheric O_3 are well characterized in their vertical extents, including: large aphelion (L_S = 40-120°) increases in low-to-mid latitude O_3 abundances over 20-50 km altitudes, distinct high latitude (> ±55°), high altitude (40-55 km) peaks in O_3 abundances during equinoctial seasons (centred on L_S = 0,180°), and very large perihelion O_3 decreases over the extended atmosphere. The aphelion increases and perihelion decreases are generally consistent with model predictions of global variation in water vapor saturation altitudes (hygropause) as driven by the elliptical Mars orbit and accentuated by perihelion dust storm heating of the extended atmosphere. During perihelion, the relative vertical abundance of O_3 and H_2O increases below ~40 km towards the surface, with both species having peak abundances at similar altitudes close to the surface; during aphelion, the same general trend applies, but with well-defined decreases in O_3 abundances present in the profiles at altitudes of 20-30 km, coincident with local peaks in H_2O.

The high latitude, equinoctial peaks in O_3 at 40-55 km altitudes, which have not been identified in previous observations, are most likely produced through a combination of anti-correlation with water vapour, and the transport of O and H atoms from equatorial regions through equinoctial meridional circulation, though the relative contribution of each process is not known. The equinoctial O_3 peaks are present in the data assimilation modelling but with much reduced peak densities. In general, modelled O_3 densities are far lower than NOMAD observed O_3 densities, most likely due to water saturation conditions being inadequately constrained in the model. An in-progress objective of assimilating NOMAD water profile measurements should provide the most diagnostic photochemical analysis of martian O_3, necessary to accurately represent the formation and distribution of O_3 on Mars.

Data availability

Public access to all ExoMars TGO data are available through the ESA Planetary Science Archive (archives.esac.esa.int/psa/) with additional access to NOMAD data through the PI institute (nomad.aeronomie.be). The derived ozone retrieval data dataset and the modelling and assimilation data that support the plots within this paper are available freely through the Open University Research Data Online (ORDO) repository at https://ordo.open.ac.uk/collections/NOMAD-UVIS/5269202 (DOI: https://doi.org/10.21954/ou.rd.13580336).

Acknowledgments

The NOMAD experiment is led by the Royal Belgian Institute for Space Aeronomy (IASB-BIRA), with Co-PI teams in the United Kingdom (Open University), Spain (IAA-CSIC) and Italy (INAF-IAPS). This work was enabled through UK Space Agency grants ST/V002295/1, ST/P001262/1, ST/V005332/1, ST/S00145X/1 and ST/R001405/1, and this project acknowledges funding by the Belgian Science Policy Office (BELSPO), with the financial and contractual coordination by the ESA Prodex Office (PEA 4000103401, 4000121493), by Spanish Ministry of Science and Innovation (MCIU) and by European funds under grants PGC2018-101836-B-I00 and ESP2017-87143-R (MINECO/FEDER), as well as by the Italian Space Agency through grant 2018-2-HH.0. This work was supported by the Belgian Fonds de la Recherche Scientifique – FNRS under grant number 30442502 (ET_HOME). S. A. is "Chargé de Recherches" at the F.R.S.-FNRS. SR thanks BELSPO for the FED-tWIN funding (Prf-2019-077 - RT-MOLEXO). The IAA/CSIC team acknowledges financial support from the State Agency for Research of the Spanish MCIU through the 'Center of Excellence Severo Ochoa' award for the Instituto de Astrofísica de Andalucía (SEV-2017-0709). US investigators were supported by the National Aeronautics and Space Administration.

References

Aoki, S., Vandaele, A. C., Daerden, F., Villanueva, G. L., Liuzzi, G., Thomas, I. R., et al. (2019). Water vapor vertical profile on Mars in dust storms observed by TGO/NOMAD. *Journal of Geophysical Research: Planets*, 124, 3482-3497. https://doi.org/10.1029/2019JE006109

Anbar, A., Leu, M.-T., Nair, H., Yung, Y., 1993. Adsorption of ho x on aerosol surfaces: Implications for the atmosphere of mars. *Journal of Geophysical Research: Planets* 98 (E6), 10933–10940.

Atreya, S., Blamont, J., 1990. Stability of the martian atmosphere: Possible role of heterogeneous chemistry. Geophysical research letters 17 (3), 287– 290.

Auvinen, H.; Oikarinen, L.; Kyrölä, E. (2002), Inversion algorithms for recovering minor species densities from limb scatter measurements at UV-visible wavelengths, *J. Geophys. Res. (Atmospheres)*, 107, D13, DOI 10.1029/2001JD000407.

Barnes, J., Haberle, R., Wilson, R., Lewis, S., Murphy, J., & Read, P. (2017). The Global Circulation. In R. Haberle, R. Clancy, F. Forget, M. Smith, & R. Zurek (Eds.), The Atmosphere and Climate of Mars (Cambridge Planetary Science, pp. 229-294). Cambridge: Cambridge University Press. doi:10.1017/9781139060172.009

Barth, C. A. & Hord, C. W. 1971. Mariner ultraviolet spectrometer: Topography and polar cap. *Science* 173, 197–201 (1971).

Barth, C. A., Hord, C. W., Stewart, A. I., Lane, A. L., Dick, M. L., Anderson, G. P., 1973. Mariner 9 ultraviolet spectrometer experiment: Seasonal variation of ozone on mars. *Science* 179 (4075), 795–796.

Benson, J. L., Kass, D. M., Kleinboehl, A., 2011. Mars' north polar hood as observed by the mars climate sounder. *Journal of Geophysical Research: Planets* 116 (E3).

Benson, J. L., Kass, D. M., Kleinboehl, A., McCleese, D. J., Schofield, J. T., Taylor, F. W., 2010. Mars' south polar hood as observed by the mars climate sounder. *Journal of Geophysical Research: Planets* 115 (E12).

Bertaux, J.-L., Fonteyn, D., Korablev, O., Chassefi`ere, E., Dimarellis, E., Dubois, J. P., Hauchecorne, A., Cabane, M., Rannou, P., Levasseur- Regourd, A. C., Cernogora, G., Quemerais, E., Hermans, C., Kockarts, G., Lippens, C., Maziere, M. D., Moreau, D., Muller, C., Neefs, B., Simon, P. C., Forget, F., Hourdin, F., Talagrand, O., Moroz, V. I., Rodin, A., Sandel, B., Stern, A., 2000. The study of the martian atmosphere from top to bottom with spicam light on mars express. *Planetary and Space Science* 48 (12), 1303–1320.

Bertaux, J.-L., Korablev, O., Perrier, S., Qu´emerais, E., Montmessin, F., Leblanc, F., Lebonnois, S., Rannou, P., Lef`evre, F., Forget, F., Fedorova, A., Dimarellis, E., Reberac, A., Fonteyn, D., Chaufray, J. Y., Guibert, S., 2006. Spicam on mars express: Observing modes and overview of uv spectrometer data and scientific results. *Journal of Geophysical Research: Planets* 111 (E10).

Blamont, J., Chassefiere, E., Goutail, J., Mege, B., Nunes-Pinharanda, M., Souchon, G., Krasnopolsky, V., Krysko, A., Moroz, V., 1991. Vertical profiles of dust and ozone in the martian atmosphere deduced from solar occultation measurements. *Planetary and Space Science* 39 (1), 175 – 187.

Blamont, J. E., Chassefi`ere, E., 1993. First detection of ozone in the middle atmosphere of mars from solar occultation measurements. *Icarus* 104 (2), 324–336.

Clancy, R. T., Nair, H., 1996. Annual (perihelion-aphelion) cycles in the photochemical behavior of the global mars atmosphere. *Journal of Geophysical Research: Planets* 101 (E5), 12785–12790.

Clancy, R.T., A.W. Grossman, M.J. Wolff, P.B. James, Y.N. Billawala, B.J. Sandor, S.W. Lee, and D.J. Rudy, 1996. Water vapor saturation at low altitudes around Mars aphelion: A key to Mars climate?, *Icarus*, **122**, 36-62.

Clancy, R. T., Wolff, M. J. & James, P. B. 1999. Minimal aerosol loading and global increases in atmospheric ozone during the 1996-1997 Martian northern spring season. *Icarus* 138, 49-63.

Clancy, R.T., B. J. Sandor, M. J. Wolff, M. D. Smith, F. Lefévre, J.-B. Madeleine, F. Forget, S. L. Murchie, F. P. Seelos, K. D. Seelos, H. A. Nair, A. D. Toigo, D. M. Kass, A. Kleinböhl, and N. Heavens, 2012. Extensive MRO CRISM Observations of 1.27 **μ**m O_2 Airglow in Mars Polar Night and Their Comparison to MRO MCS Temperature Profiles and LMD GCM Simulations, *J. Geophys. Res*., **117**, E00J10, doi:10.1029/2011JE004018.

Clancy, R. T., Sandor, B. J., García-Muñoz, A., Lefèvre, F., Smith, M. D., Wolff, M. J., Montmessin, F., Murchie, S. L., and Nair, H., 2013, First detection of Mars atmospheric hydroxyl: CRISM near-IR measurement versus LMD GCM simulation of OH Meinel band emission in the Mars polar winter atmosphere, *Icarus*, 226, 272-281.

Clancy, R. T., Wolff, M. J., Lefèvre, F., Cantor, B. A., Malin, M. C., Smith, M. D., 2016. Daily global mapping of mars ozone column abundances with marci uv band imaging. *Icarus* 266, 112–133.

Clancy, R. T., Smith, M. D., Lefèvre, F., McConnochie, T. H., Sandor, B. J., Wolff, M. J., S. W. Lee, Murchie, S. L., Toigo, A. D., Nair, H., and Navarro, T., 2017. Vertical profiles of Mars 1.27 μm O_2 dayglow from MRO CRISM limb spectra: seasonal/global behaviors, comparisons to LMDGCM simulations, and inferences on Mars water vapor distributions, *Icarus*, **293**, 132-156.

Colaïtis, A., Spiga, A., Hourdin, F., Rio, C., Forget, F., Millour, E., 2013. A thermal plume model for the Martian convective boundary layer. *J. Geophys. Res*. 118, 1468–1487.

Daerden, F., Neary, L., Viscardy, S., García Muñoz, A., Clancy, R. T., Smith, M. D., Encrenaz, T., and Fedorova, F., 2019, Mars atmospheric chemistry simulations with the GEM-Mars general circulation model, *Icarus* 326, 197-224.

Encrenaz, T., Greathouse, T. K., Aoki, S., Daerden, F., Giuranna, M., Forget, F., Lefèvre, F., Montmessin, F., Fouchet, T., Bézard, B., Atreya, S., DeWill, C., Richter, M. J., Neary, L., and Viscardy, S., 2019, Ground-based infrared mapping of H_2O_2 on Mars near opposition, *Astron. and Astrophys*., 627 (A60), 1-10.

Fast, K., Kostiuk, T., Espenak, F., Annen, J., Buhl, D., Hewagama, T., A'Hearn, M. F., Zipoy, D., Livengood, T. A., Sonnabend, G., Schmuelling, F., 2006. Ozone abundance on mars from infrared heterodyne spectra: I. acquisition, retrieval, and anticorrelation with water vapor. *Icarus* 181 (2), 419–431.

Fedorova, A., Bertaux, J.-P., Betsis, D., Montmessin, F., Korablev, O., Maltagliati, L., and Clarke, J., 2018, Water vapor in the middle atmosphere of Mars during the 2007 global dust storm, *Icarus* 200, 440-457.

Fedorova, A., Montmessin, F., Korablev, O., Luginin, M., Trokhimovskiy, A., Belyaev, D. A., et al. (2020). Stormy water on Mars: The distribution and saturation of atmospheric water during the dusty season. *Science*, 367, 297–300.

Fedorova, A., Korablev, O., Perrier, S., Bertaux, J.-L., Lef`evre, F., Rodin, A., 2006. Mars water vapor abundance from SPICAM IR spectrometer: Seasonal and geographic distributions, *Journal Geophys. Res*. 111, E09S08.

Forget, F., Hourdin, F., Fournier, R.,Hourdin, C., Talagrand, O., Collins, M., Lewis, S.R., Read, P.L. and Huot, J.P. (1999), Improved general circulation models of the martian atmosphere from the surface to above 80 km, *Journal of Geophysical Research: Planets*, 104(E10):24155-24175.

Guzewich, S. D., Lemmon, M., Smith, C.L., Martínez, G., de Vicente-Retortillo, Á., Newman, C. E., et al. (2019). Mars Science Laboratory observations of the 2018/Mars year 34 global dust storm. *Geophysical Research Letters*, 46, 71–79. https://doi.org/10.1029/2018GL080839

Hartley, W., 1881. Xxi.—on the absorption of solar rays by atmospheric ozone. *Journal of the Chemical Society, Transactions* 39, 111–128.

Heavens N.G., Kleinböhl A., Chaffin M.S., Halekas J.S., Kass D.M., Hayne P.O., McCleese D.J., Piqueux S., Shirley J.H., Schofield J.T. (2018). Hydrogen escape from Mars enhanced by deep convection in dust storms. *Nature Astronomy*, 2 (2018), pp. 126-132, 10.1038/s41550-017-0353-4

Holmes, J. A., Lewis, S. R., Patel, M. R., 2017. On the link between martian total ozone and potential vorticity. *Icarus* 282, 104–117.

Holmes, J.A., Lewis, S.R., Patel, M.R., and Lefèvre, F. (2018), A reanalysis of ozone on Mars from assimilation of SPICAM observations, *Icarus*, 302, 308-318.

Holmes, J.A., Lewis, S.R., Patel, M.R., Smith, M.D., 2019. Global analysis and forecasts of carbon monoxide on Mars. *Icarus* 328, 232–245.

Holmes, J.A., Lewis, S.R., and Patel, M.R (2020), OpenMARS: A global record of martian weather from 1999-2015 (2020), *Planetary and Space Science*, 188, 1049462.

Jakosky, B. M., and Farmer, C. B., 1982, The seasonal and global behavior of water vapor in the Mars atmosphere: Complete global results of the Viking Atmospheric Water Detector Experiment, *Journal of Geophysical Research*, 87, 2999-3019.

Kass, D. M., Kleinböhl, A., McCleese, D. J., Schofiled, J. T., and Smith, M. D., 2016. Interannual similarity in the Martian atmosphere during the dust storm season, *Geophys. Res. Lett* 43, 6111-6118.

Khayat, A.S.J, M.D. Smith, M.J. Wolff, F. Daerden, L. Neary, M.R. Patel, A. Piccialli, A.C. Vandaele, I.R. Thomas, B. Ristic, J.P. Mason, Y. Willame, C. Depiesse, G. Bellucci, J.J. López-Moreno, and the NOMAD team. The high-altitude peaks of atmospheric ozone as observed by NOMAD/UVIS onboard the ExoMars Trace Gas Orbiter Mission. *Journal of Geophysical Research- Planets*, this issue.

Kleinböhl, A., Friedson, A.J., Schofield, J.T., 2017. Two-dimensional radiative transfer for the retrieval of limb emission measurements in the Martian atmosphere. *J. Quant. Spectrosc. Radiat. Transf.* 187, 511–522.

Korablev, O., et al., 2019, No detection of methane on Mars from early ExoMars Trace Gas Orbiter observations, *Nature,* **568**, 517-520.

Korablev, O., et al., 2020, Transient HCl in the atmosphere of Mars, *Science*, in review.

Krasnopolsky, V., 1993. Photochemistry of the martian atmosphere (mean conditions). *Icarus* 101 (2), 313 – 332.

Lebonnois, S., Qu´emerais, E., Montmessin, F., Lef`evre, F., Perrier, S., Bertaux, J.-L., Forget, F., 2006. Vertical distribution of ozone on mars as measured by spicam/mars express using stellar occultations. *Journal of Geophysical Research: Planets* 111 (E9).

Lefèvre, F., Lebonnois, S., Montmessin, F., Forget, F., 2004. Three- dimensional modeling of ozone on mars. *Journal of Geophysical Research: Planets* 109 (E7).

Lefèvre, F., Bertaux, J.-L., Clancy, R. T., Encrenaz, T., Fast, K., Forget, F., Lebonnois, S., Montmessin, F., Perrier, S., 2008. Heterogeneous chemistry in the atmosphere of Mars. *Nature* 454, 971.

Lefèvre, F., and Krasnopolsky, V., 2017, Atmospheric photochemistry. In: Haberle, Robert M., Todd Clancy, R., François Forget, Smith Richard, Michael D., Zurek, W. (Eds.), The Atmosphere and Climate of Mars. Cambridge University Press, pp. 405–432 (chapter 13).

Lemoine, F. G., Smith, D. E., Rowlands, D. D., Zuber, M. T., Neumann, G. A., Chinn, D. S., & Pavlis, D. E. (2001). An improved solution of the gravity field of Mars (GMM-2B) from Mars Global Surveyor. *Journal of Geophysical Research*, 106(E10), 23,359–23,376. https://doi.org/10.1029/2000JE001426

Lewis, S.R., Barker, P.R., 2005. Atmospheric tides in a Mars general circulation model with data assimilation. *Adv. Space Res*. 36, 2162–2168.

Lewis, S.R., Read, P.L., Conrath, B.J., Pearl, J.C., and Smith, M.D. (2007), Assimilation of thermal emission spectrometer atmospheric data during the mars global surveyor aerobraking period, *Icarus*, 192(2):327-347.

Liuzzi, G., Villanueva, G. L., Crismani, M. M. J., Smith, M. D., Mumma, M. J., Daerden, F., et al. (2020). Strong variability of Martian water ice clouds during dust storms revealed from ExoMars Trace Gas Orbiter/NOMAD. *Journal of Geophysical Research: Planets*, 124. https://doi.org/10.1029/2019JE006250

Malicet, J., D. Daumont, J. Charbonnier, C. PArisse, A. Chakir and J. Brion, Ozone UV Spectroscopy. II. Absorption Cross-Sections and Temperature Dependence, *J. Atmos. Chem*. 21, 263-273, 1995.

Maltagliati, L., Montmessin, Fedorova, A., Korablev, O., Forget, F., and Bertaux, J.-L., 2011. Evidence of water vapor in excess of saturation in the atmosphere of Mars, *Science* 333, 1868-1870.

Maltagliati, L., Montmessin, F., Korablev, O., Fedorova, A., Forget, F., Määttänen, A., Lefèvre, F., Bertaux, J.-L., 2013. Annual survey of water vapor vertical distribution and water-aerosol coupling in the martian atmosphere observed by SPICAM/MEx solar occultations. *Icarus* 223, 942–962.

Marmo, F. F., Shardanand, Warneck, P., 1965. Ozone distribution in the atmosphere of mars. *Journal of Geophysical Research* 70 (9), 2270–2272.

Mateshvili, N., Fussen, D., Vanhellemont, F., Bingen, C., Dodion, J., Montmessin, F., Perrier, S., Dimarellis, E., Bertaux, J.-L., 2007. Martian ice cloud distribution obtained from spicam nadir uv measurements. *Journal of Geophysical Research: Planets* 112 (E7).

McElroy, M. B., Donahue, T. M., 1972. Stability of the martian atmosphere. *Science* 177 (4053), 986–988.

Modak, A., Sheel, V., Lefèvre, F., 2019a. Competing pathways in oxygen photochemistry of the martian atmosphere. *Planetary and Space Science*, 104783. https://doi.org/10.1016/j.pss.2019.104783

Modak, A., Sheel, V., Montmessin, F., 2019b. Retrieval of martian ozone and dust from spicam spectrometer for my27–my28. *Journal of Earth System Science* 128 (6), 144.

Montabone, L., Lewis, S.R., Read, P.L., Hinson, D.P., 2006. Validation of Martian meteorological data assimilation for MGS/TES using radio occultation measurements. *Icarus* 185, 113–132.

Montabone, L., Marsh, K., Lewis, S.R., Read, P.L., Smith, M.D., Holmes, J., Spiga, A., Lowe, D., Pamment, A., 2014. The mars analysis correction data assimilation (MACDA) dataset V1.0. *Geosci. Data J.* 1 (2), 129–139.

Montabone L., Spiga A., Kass D. M., Kleinböhl A., Forget F., Millour E. (2020). Martian Year 34 Column Dust Climatology from Mars Climate Sounder Observations: Reconstructed Maps and Model Simulations. *Journal of Geophysical Research: Planets*. https://doi-org/10.1029/2019je006111.

Montmessin, F., Forget, F., Rannou, P., Cabane, M., and Haberle, R. M., 2004, *Journal of Geophysical Research* 109 (E10004), 1-26.

Montmessin, F., Korablev, O., Lef˙evre, F., Bertaux, J.-L., Fedorova, A., Trokhimovskiy, A., Chaufray, J., Lacombe, G., Reberac, A., Maltagliati, L., Willame, Y., Guslyakova, S., G´erard, J.-C., Stiepen, A., Fussen, D., Mateshvili, N., M¨a¨att¨anen, A., Forget, F., Witasse, O., Leblanc, F., Vandaele, A., Marcq, E., Sandel, B., Gondet, B., Schneider, N., Chaffin, M., Chapron, N., 2017. Spicam on mars express: A 10 year in-depth survey of the martian atmosphere. *Icarus* 297, 195 – 216.

Montmessin, F., Lefèvre, F., 2013. Transport-driven formation of a polar ozone layer on Mars. *Nature Geoscience*, 6, 930.

Nair, H., Allen, M., Anbar, A. D., Yung, Y. L., Clancy, R., 1994. A photochemical model of the martian atmosphere. *Icarus* 111 (1), 124 – 150.

Navarro, T., Madeleine, J.-B., Forget, F., Spiga, A., Millour, E., Montmessin, F., Määttänen, A., 2014. Global climate modeling of the Martian water cycle with improved microphysics and radiatively active water ice clouds. *J. Geophys. Res. Planets* 119, 1479–1495.

Neary, L., Daerden, F., Aoki, S., Whiteway, J., Clancy, R. T., Smith, M., Viscardy, S., Erwin, J. T., Thomas, I. R., Villanueva, G., Liuzzi, G., Crismani, M., Wolff, M., Lewis, S. R., Holmes, J. A., Patel, M. R., Giuranna, M., Depiesse, C., Picialli, A., Robert, S., Trompet, L., WIllame, Y., Ristic, B., and Vandaele, A. C., 2019, Explanation for the increase in high-altitude water on Mars observed by NOMAD during the 2018 global dust storm, *Geophys. Res. Lett*. 47 (7), 1-9.

Newman, C.E., Lewis, S.R., Read, P.L., Forget, F., 2002. Modeling the Martian dust cycle, 1. Representations of dust transport processes. *J. Geophys. Res.* 107, 5123.

Pankine, A. and Tamppari, L. K., 2019, MGS TES observations of the water vapor in the Martian southern polar atmosphere during spring and summer, *Icarus* 331, 26-48.

Patel, M.R., Antoine, P., Mason, J.P., Leese, M.R., Hathi, B., Stevens, A.H. Dawson, D., Gow, J.P.D., Ringrose, T.J. et al. (2017). NOMAD spectrometer on the ExoMars trace gas orbiter mission: part 2—design, manufacturing, and testing of the ultraviolet and visible channel. *Applied Optics*, 56(10) pp. 2771–2782.

Perrier, S., Bertaux, J. L., Lef`evre, F., Lebonnois, S., Korablev, O., Fedorova, A., Montmessin, F., 2006. Global distribution of total ozone on mars from spicam/mex uv measurements. *Journal of Geophysical Research: Planets* 111 (E9).

Quémerais, E., J.-L. Bertaux, O. Korablev, E. Dimarellis, C. Cot, B. R. Sandel, and D. Fussen (2006), Stellar occultations observed by SPICAM on Mars Express, *J. Geophys. Res*., 111, E09S04, doi:10.1029/2005JE002604.

Rodgers, C. D. (2000), Inverse Methods for Atmospheric Sounding, 238 pp., World Sci., Hackensack, N.J.

Shimazaki, T., Shimizu, M., 1979. The seasonal variation of ozone density in the martian atmosphere. *Journal of Geophysical Research: Space Physics* 84 (A4), 1269–1276.

Smith, M. D., 2004, Interannual variability in TES atmospheric observations of Mars during 1999-2003, *Icarus* 167, 148-165.

Smith, M. D., M. J. Wolff, R. T. Clancy, and S. L. Murchie, 2009. CRISM Observations of Water Vapor and Carbon Monoxide, *J. Geophys. Res.*, 114 (E9). DOI 10.1029/2008JE003288.

Smith, M.D. 2019. THEMIS observations of the 2018 Mars global dust storm. *J. Geophys. Res. Planets*, 124. doi:10.1029/2019JE006107Snow, M., Machol, J., Viereck, R.,Woods, T., Weber, M., Woodraska, D.,& Elliott, J. (2019). A revised Magnesium II core-to-wing ratio from SORCE SOLSTICE. *Earth and Space Science*, 2106 2114. https://2doi.org/10.1029/2019EA000652

Steel, L. J., Lewis, S. R., Patel, M. R., Montmessin, F., Forget, F., and Smith, M. D., 2014. The seasonal cycle of water vapour on Mars from assimilation of Thermal Emission Spectrometer data, *Icarus* 237, 91-115.

Streeter, P.M., Lewis, S.R., Patel, M.R., Holmes, J.A., and Kass, D.M (2020), Surface warming during the 2018/mars year 34 global dust storm, *Geophysical Research Letters*, 47(9):e2019GL083936.

Trompet, L., Mahieux, A., Ristic, B., Robert, S., Wilquet, V., Thomas, I. R., et al. (2016). Improved algorithm for the transmittance estimation of spectra obtained with SOIR/Venus Express. *Applied Optics*, 55(32), 9275. https://doi.org/10.1364/AO.55.009275

Vandaele, A. C., Lopez-Moreno, J.-J., Patel, M. R., Bellucci, G., Allen, M., Alonso-Rodrigo, G., et al., & the NOMAD Team (2018). NOMAD, an integrated suite of three spectrometers for the ExoMars Trace Gas mission: technical description, science objectives and expected performance. *Space Science Reviews*, 214(5). https://doi.org/10.1007/s11214-018-0517-2

Wolff, M. J., Clancy, R. T., Kahre, M. A., Haberle, R. M., Forget, F., Cantor, B. A., Malin, M. C., 2019. Mapping water ice clouds on Mars with MRO/MARCI. *Icarus*, 332. https://doi.org/10.1016/j.icarus.2019.113512.

Vandaele, A. C., et al., 2018, NOMAD, an Integrated Suite of Three Spectrometers for the ExoMars Trace Gas Mission: Technical Description, Science Objectives and Expected Performance, *Space Sci. Rev.*, **214:80**, doi.org/10.1007/s11214-018-0517-2.

Vandaele et al., 2019, Martian dust storm impact on atmospheric H_2O and D/H observed by ExoMars Trace Gas Orbiter, *Nature*, **568**, 521-525.